iScience

CellPress
OPEN ACCESS

Article

Site-specific phosphorylation of PSD-95 dynamically regulates the postsynaptic density as observed by phase separation

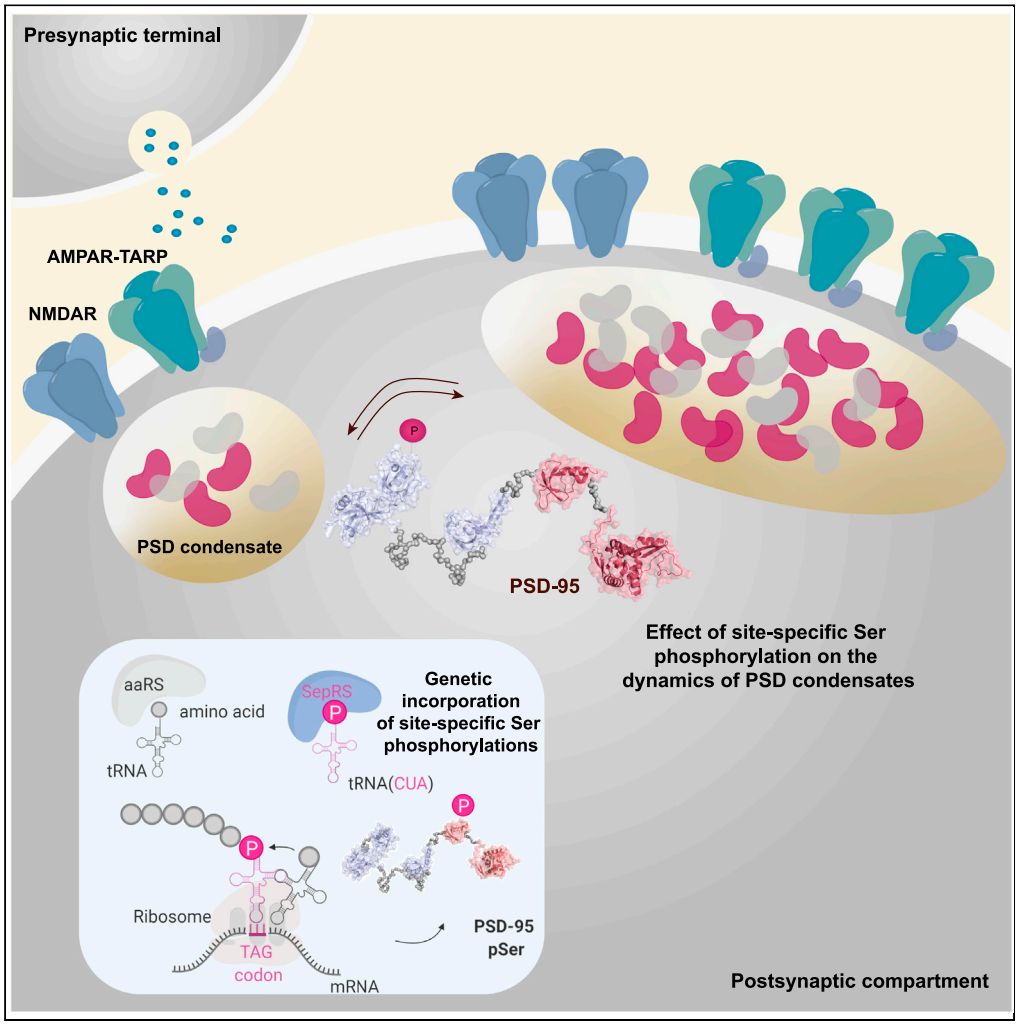

Genetic incorporation of Ser phosphorylations in PSD and the effect on the dynamics of PSD condensates.

Maria Vistrup-Parry, Xudong Chen, Thea L. Johansen, ..., Michael L. Nielsen, Mingjie Zhang, Kristian Strømgaard

kristian.stromgaard@sund.ku.dk

Highlights

Genetically introduced site-specific pSer in single, tandem and full-length PSD-95

The inserted pSer residues altered the PSD dynamics as shown by phase separation

Phosphorylation of Ser78 in PSD-95 inhibited phase separation with GluN2B and Stg

Phosphorylation of Ser116 in PSD-95 promoted phase separation with Stg only

Vistrup-Parry et al., iScience *24*, 103268
November 19, 2021
https://doi.org/10.1016/j.isci.2021.103268

iScience

CellPress
OPEN ACCESS

Article

Site-specific phosphorylation of PSD-95 dynamically regulates the postsynaptic density as observed by phase separation

Maria Vistrup-Parry,[1] Xudong Chen,[2] Thea L. Johansen,[1] Sofie Bach,[1] Sara C. Buch-Larsen,[3] Christian R.O. Bartling,[1] Chenxue Ma,[2] Louise S. Clemmensen,[1,5] Michael L. Nielsen,[3] Mingjie Zhang,[2,4] and Kristian Strømgaard[1,6,*]

SUMMARY

Postsynaptic density protein 95 is a key scaffolding protein in the postsynaptic density of excitatory glutamatergic neurons, organizing signaling complexes primarily via its three PSD-95/Discs-large/Zona occludens domains. PSD-95 is regulated by phosphorylation, but technical challenges have limited studies of the molecular details. Here, we genetically introduced site-specific phosphorylations in single, tandem, and full-length PSD-95 and generated a total of 11 phosphorylated protein variants. We examined how these phosphorylations affected binding to known interaction partners and the impact on phase separation of PSD-95 complexes and identified two new phosphorylation sites with opposing effects. Phosphorylation of Ser78 inhibited phase separation with the glutamate receptor subunit GluN2B and the auxiliary protein stargazin, whereas phosphorylation of Ser116 induced phase separation with stargazin only. Thus, by genetically introducing phosphoserine site-specifically and exploring the impact on phase separation, we have provided new insights into the regulation of PSD-95 by phosphorylation and the dynamics of the PSD.

INTRODUCTION

The postsynaptic density protein 95 (PSD-95) is one of the most abundant proteins in the postsynaptic density (PSD) of excitatory glutamatergic neurons (Zhu et al., 2016). PSD-95 interacts with receptors, ion channels, and intracellular proteins, thereby organizing signaling complexes critical for synaptic development and transmission (Feng and Zhang, 2009; Kim and Sheng, 2004). At the plasma membrane, PSD-95 interacts with the glutamate receptor subtypes α-amino-hydroxy-5-methyl-4-isoxazolepropionic acid (AMPA) receptor through its auxiliary subunit stargazin (Stg) (Chen et al., 2000; El-Husseini et al., 2000; Nicoll et al., 2006) and directly with the C-terminal of the *N*-methyl-D-aspartate (NMDA) receptor (Niethammer et al., 1996; Kornau et al., 1995), among others. Furthermore, it interacts with components of the PSD and signaling proteins such as neuronal nitric oxide synthase (nNOS) (Aarts et al., 2002; Pedersen et al., 2014; Sattler et al., 1999). PSD-95 has been implicated in postsynaptic development, as it is one of the first proteins to cluster at synapses (Funke et al., 2005; Rao et al., 1998). Moreover, mutations in PSD-95 have been identified as associated with diseases such as stroke, as well as with intellectual disability, autism spectrum disorder, and schizophrenia (Coley and Gao, 2018; Volk et al., 2015).

PSD-95 belongs to the family of membrane-associated guanylate kinase (MAGUK) proteins and contains three PSD-95/Discs-large/Zona occludens (PDZ) domains along with a Src Homology 3 (SH3) and a guanylate kinase (GK) domain (Figure 1A) (Chen et al., 2015). PDZ domains are one of the largest classes of protein-protein interaction (PPI) modules, and the vast majority of PSD-95 mediated interactions are attributed to the three PDZ domains (Lee and Zheng, 2010; Ye and Zhang, 2013). PDZ domains are comprised of approximately 90 amino acids arranged in a specific globular fold (Doyle et al., 1996), and more than 250 human proteins have been acknowledged to contain PDZ domains (Ye and Zhang, 2013). In the canonical binding mode, PDZ domains bind the extreme carboxy-terminal of the protein interaction partner (Chi et al., 2012; Doyle et al., 1996; Kim et al., 1995), characterized by the consensus

[1]Center for Biopharmaceuticals, Department of Drug Design and Pharmacology, University of Copenhagen, Jagtvej 162, 2100 Copenhagen, Denmark

[2]Division of Life Science, State Key Laboratory of Molecular Neuroscience, Hong Kong University of Science and Technology, Clear Water Bay, Kowloon, Hong Kong, China

[3]Proteomics Program, Novo Nordisk Foundation Center for Protein Research, University of Copenhagen, Blegdamsvej 3B, 2200 Copenhagen, Denmark

[4]Shenzhen Bay Laboratory, Gaoke Innovation Center, Guangqiao Road, Guangming District, Shenzhen, China

[5]Present address: BioInnovation Institute, Ole Maaløes Vej 3, 200 Copenhagen, Denmark

[6]Lead contact

*Correspondence: kristian.stromgaard@sund.ku.dk

https://doi.org/10.1016/j.isci.2021.103268

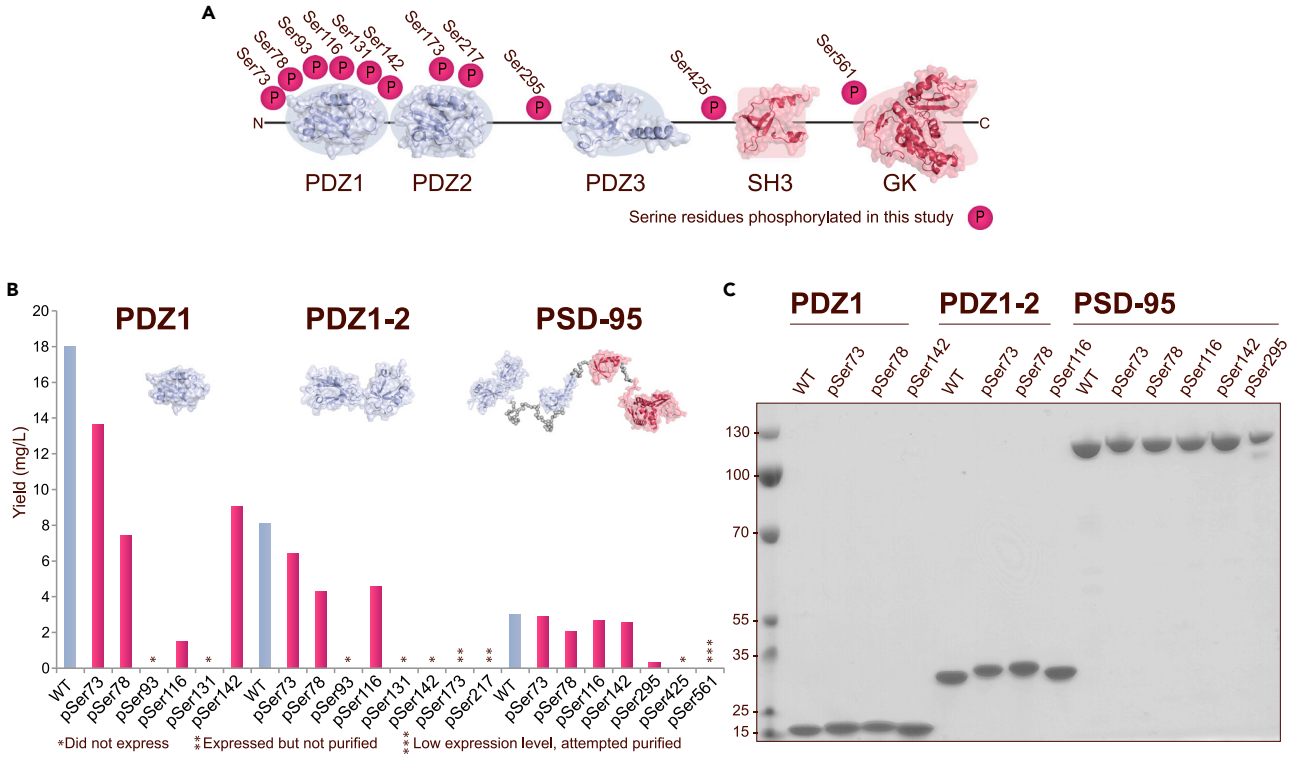

Figure 1. Site-specific phosphorylation of PSD-95

(A) The organization of the five domains in PSD-95 (PDZ1-3, SH3, and GK). The Ser residues attempted phosphorylated in this study are highlighted by a phosphorylation icon. Using the software Ranch, a model of PSD-95 was generated using known structural domains of PSD-95 connected via a fully flexible linker (PDZ1-2, PDB: 3GSL [Sainlos et al., 2011]; PDZ3, PDB: 5JXB [Zeng et al., 2016]; SH3-GK, PDB: 1KJW [McGee et al., 2001]).

(B) Histogram depicting all sites attempted phosphorylated and the yield (mg/L) of purification for purified proteins for all three protein forms. Proteins that did not express are indicated by *, proteins that expressed but have not been purified by **, and proteins with low expression and attempted purified with ***.

(C) Coomassie stained gel of all purified pSer protein variants loaded alongside a protein ladder.

sequence S/T-X-Φ-OH, where X is any amino acid and Φ is a hydrophobic amino acid. Some PDZ domains although confer noncanonical binding of internal peptide motifs (Harris et al., 2001).

PPIs generally play essential roles in all aspects of cellular function by mediating signal transduction and metabolism, and because of many diseases being linked to malfunctioning signaling, PPIs have been explored as drug targets. In particular, the PDZ-mediated interactions between PSD-95, NMDA receptors, and nNOS have been explored in the treatment of ischemic stroke, and two inhibitors of PSD-95, NA-1 (nerinetide) and AVLX-144, are currently in different stages of clinical trials (Bach et al., 2012; Hill et al., 2012).

The PSD was first visualized by electron microscopy (EM) as an electron-dense thickening below the plasma membrane (Gray, 1959). Since, the organization of the PSD has been shown to constitute multiple proteins in addition to PSD-95, which anchors proteins in the plasma membrane to the cytoskeleton (Chen et al., 2011; Sheng and Hoogenraad, 2007; Sheng and Kim, 2011). The dynamics of the PSD have been challenging to study, as the PSD is a protein-rich membrane-less compartment that assembles and disassembles continuously (Hyman et al., 2014; Zeng et al., 2016). Furthermore, synapses are dynamic and plastic, and hence, the morphology of two neighboring synapses can differ significantly (Nishiyama and Yasuda, 2015; Zeng et al., 2018a). However, recently the PSD was reconstituted and subsequently studied using liquid-liquid phase separation (LLPS) (Zeng et al., 2018a). Here, the reconstituted PSD, consisting of PSD-95, guanylate kinase-associated protein (GKAP), SH3 and multiple ankyrin repeat domain protein (Shank), and Homer protein homolog 3 (Homer3), was able to cluster subunits of the NMDA receptor, enrich synaptic enzymes, and promote actin bundle formation. Hence this model system proved to be a highly promising approach for studying the interactions of the PSD (Zeng et al., 2018a).

PSD-95 is vastly regulated by phosphorylation, thereby affecting synaptic activity (Gardoni et al., 2006; Vallejo et al., 2016). The first PDZ domain (PDZ1) of PSD-95 contains six Ser residues, and as Ser is the most prevalent acceptor residue of protein phosphorylation, multiple of these residues have been identified by mass spectrometry (MS)-based approaches to be phosphorylated (Ballif et al., 2008; Xue et al., 2008). Among these, Ser73 has been shown to be phosphorylated by CaMKIIα (Gardoni et al., 2006). Phosphorylation of PSD-95 has also been studied by employing kinases capable of phosphorylating PSD-95 and subsequently identifying modified sites (Chetkovich et al., 2002; Du et al., 2009; Morabito et al., 2004); however, this approach has restricted site specificity and requires prior knowledge of the implicated kinases. We have previously introduced site-specific phosphorylations in single PDZ domains of PSD-95 by semisynthetic strategies and studied the effect by biochemical binding assays to a large library of C-terminal peptide interaction partners (Pedersen et al., 2017). This demonstrated how specific phosphorylations fine-tune regulation of interactions with the NMDA receptor and Stg. However, limitations of the semisynthetic approach prevented the exploration of the effect of phosphorylation on interdomain interactions found in the full-length (FL) of PSD-95. Recently, we showed that the tandem PDZ1-2 of PSD-95 was necessary for phase separation with Stg, as single PDZ domains alone did not phase separate with Stg (Zeng et al., 2019); this illustrates the importance of interdomain interactions in the molecular mechanisms of PSD proteins.

The ability to site-specifically phosphorylate Ser residues genetically by amber codon suppression has provided the necessary means for studying phosphorylation of larger proteins (Rogerson et al., 2015; Xie and Schultz, 2005). Here, we use amber codon suppression to site-specifically phosphorylate multiple Ser residues in PSD-95. We show that we can site-specifically phosphorylate multiple positions in single (PDZ1), tandem (PDZ1-2), and FL PSD-95, also revealing that some sites are more prone to amber codon suppression than others with differences found on both site and protein level. We furthermore study the effect of phosphorylation on the dynamics of the PSD, both by biochemical binding assays and by LLPS. In the latter, we show that the interdomain interactions of FL PSD-95 affect the phase separation with protein ligands. This supports the importance of studying FL proteins in contrast to single domains, as the contribution of multivalent interactions is acknowledged. By combining genetically encoded site-specific phosphorylations with phase separation studies, we provided a novel way to study the effect of phosphorylation on the dynamics of the PSD.

RESULTS

Site-specific phosphorylation of PSD-95

To explore the feasibility of genetically introducing phosphoserine (pSer) in PSD-95, we first aimed to introduce pSer at all six Ser positions of PDZ1 in the PDZ1 single and PDZ1-2 tandem proteins of PSD-95 (Figure 1A). To do this, *Escherichia coli* BL21Δ*serB* cells were co-transformed with the previously described single high-copy plasmid pKW2 EF-Sep (Rogerson et al., 2015) and plasmids carrying the protein coding sequences containing an amber (TAG) codon at the desired positions (Table S1). The pKW2 EF-Sep plasmid contains the optimized aminoacyl tRNA synthetase and tRNA pair SepRS(2)/pSer $tRNA(B4)_{CUA}$ specific for pSer incorporation and orthogonal to the endogenous synthetase and tRNA pairs of *E coli*, which are responsible for incorporating the remaining natural amino acids into the proteins. The plasmid furthermore contains the elongation factor (EF)-Sep optimized for pSer incorporation (Park et al., 2011; Rogerson et al., 2015). The *E coli* used for protein expression, BL21Δ*serB*, lack phosphoserine phosphatase, preventing cleavage of the introduced phosphorylated amino acid while also maintaining an intracellular pool of pSer (Park et al., 2011). For the incorporation, 1 mM pSer was added to the media, and upon induction with 0.5 mM isopropyl β-D-1-thiogalactopyranoside (IPTG), phosphorylated variants of PDZ1 and PDZ1-2 were expressed and pSer introduced at the desired positions in response to the TAG codons.

We successfully introduced pSer at four different positions in PDZ1 and PDZ1-2 (Figures 1B and 1C). Ser73 and Ser78 were site-specifically phosphorylated in both PDZ1 and PDZ1-2 and the proteins purified in high yields (Figure 1B). Interestingly, two positions were only successfully phosphorylated in either one of the two protein variants, Ser142 in PDZ1 and Ser116 in PDZ1-2, respectively. PDZ1 pSer116 expressed as insoluble protein in inclusion bodies and purification resulted in low yield and purity, where a mixture of both WT and pSer mass was observed, thus the protein variant was excluded from further studies. Moreover, phosphorylation of Ser93 and Ser131 was not achieved in neither PDZ1 nor PDZ1-2.

The positions in PDZ1 that were successfully phosphorylated in the PDZ1 and PDZ1-2 protein variants were then attempted phosphorylated in FL PSD-95 (amino acids 60-724), from here on termed PSD-95. Here, amber codon suppression of all four positions (Ser73, Ser78, Ser116, and Ser142) resulted in expression of phosphorylated protein, albeit in lower yields (Figure 1B). PSD-95 was furthermore phosphorylated in position Ser295, which is located in the linker region between PDZ2 and PDZ3 (Figure 1A). The expression efficiency was very low, which resulted in a yield of less than 1 mg protein per liter expression culture (mg/L) (Figure 1B). Furthermore, poor efficiency of amber codon suppression at positions Ser425 and Ser561 in PSD-95 was observed, and the proteins were not purified (Figure 1B). Two positions in PDZ2 of the tandem PDZ1-2 were successfully suppressed and phosphorylated, Ser173 and Ser217, but not pursued further.

The yield of the phosphorylated protein variants of PDZ1, PDZ1-2, and PSD-95 decreased with protein size, which aligned with the observed expressions, and purification of PDZ1 WT resulted in 5-fold higher yield than PSD-95 WT (Figure 1B). A total of 14 protein variants of PDZ1, PDZ1-2, and PSD-95 were generated, 11 of these phosphorylated at five different positions (Figure 1C).

Characterization of protein variants and identification of interesting sites

The secondary structure of the proteins was evaluated by circular dichroism (CD) and the introduced phosphorylations were found not to affect the secondary structure (Figure 2A). Moreover, protein phosphorylation did not affect the stability of the protein variants, as measured by assessing the thermal denaturation of the proteins (Figure S1).

To examine the influence of the site-specific phosphorylations on binding to known interaction partners and ligands, we measured the binding affinity of PDZ1-2 and PSD-95 protein variants to the fluorescently labeled dimeric peptide inhibitor AVLX-144 (Bach et al., 2012) by fluorescence polarization (FP). In a concentration dependent manner, ligand saturation with protein was measured and binding constants (K_d) calculated (Figure 2B). Both protein variants bound the dimeric peptide inhibitor with nanomolar affinities (Table S2). All phosphorylations were observed to decrease the binding affinity to AVLX-144, and interestingly, both protein variants phosphorylated on Ser78 did not bind to AVLX-144. Ser78 is located in the carboxylate binding site of the PDZ1 domain (Figure 2C), which can explain the dramatic effect on peptide binding. Ser116 is located in the acidic surface of the PDZ1 domain, and phosphorylation of this site also resulted in reduced binding affinity of AVLX-144.

Identification of site-specific phosphorylations

The insertion of pSer was characterized as a mass change of 80 Dalton (Da) corresponding to the phosphate group and determined by liquid chromatography-mass spectrometry (LC-MS) (Figures 3 and S2–S4; Data S1). The introduction of the site-specific phosphorylations was verified by LC-coupled tandem MS (LC-MS/MS) (Figures 3 and S2–S4; Data S1). The proteins were purified to greater than 90%, as determined by reverse phase ultra-performance liquid chromatography (UPLC) (Figures S2–S4), and cleaved by enzymatic digestion in order to simplify fractionation, ionization, and fragmentation. By tandem-MS, the incorporation of pSer at all positions except pSer295 in PSD-95 was confirmed with high localization probabilities (>0.9), which is of great importance for the study of the effect of site-specific phosphorylation and validates the approach (Figures 3 and S2–S4; Table 1; Data S1). The sites furthermore displayed high intensities and delta scores, demonstrating that they were the most confident identifications in the individual samples (Table 1). Altogether, this validates the approach of genetic incorporation of pSer into PSD-95.

Effect of phosphorylation of Ser78 and Ser116 on binding to stargazin and GluN2B

To further evaluate the effect of phosphorylation, all pSer variants were analyzed for the binding to ligands by isothermal titration calorimetry (ITC) and FP assays. Through its interactions with the C-terminal of subunits of the NMDA receptor and Stg, the auxiliary subunit of the AMPA receptor, PSD-95 regulates the two most prevalent ionotropic glutamate receptors (iGluRs) at the PSD, and these interactions were the primary interactions of interest.

The effect of phosphorylation on the binding to a Stg protein ligand was measured by ITC for all protein variants. Here, the entire C-terminal tail of Stg including the PDZ-binding motif (PBM) (amino acids 203D-323 V) was employed as the protein ligand, which all proteins were observed to bind with micromolar affinities (Figures 4A, 4B, and S5). The binding affinity increased with protein size, and PSD-95 WT was observed to bind the Stg protein ligand with an affinity of 1.2 μM. This was almost a 100-fold higher

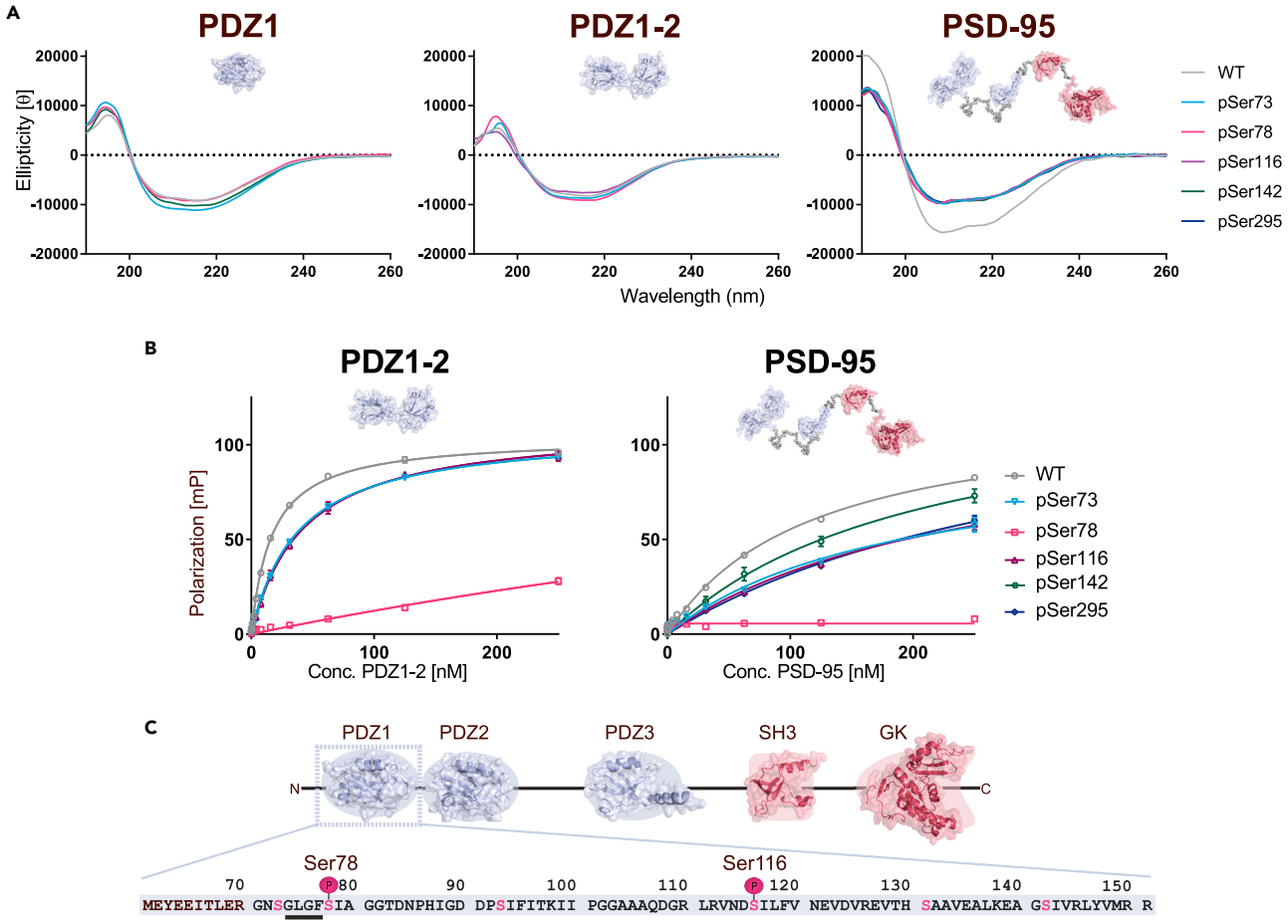

Figure 2. Characterization protein variants and identification of interesting sites

(A) CD spectra for all purified protein variants of PDZ1, PDZ1-2, and PSD-95. Three accumulated spectra were measured at 25°C from 260 to 190 nm and the molar ellipticity calculated.

(B) Protein variants of PDZ1-2 and PSD-95 were tested for binding to peptide inhibitor AVLX-144 in an FP saturation assay. Here, 10 nM of Cy5-labeled AVLX-144 was saturated with protein in a concentration-dependent manner with a maximum concentration of 250 nM protein. The milli-polarization (mP) was measured for all concentrations in triplicates, background fluorescence subtracted, and the data fitted to a one-sided binding model from which Kd values were calculated. Data are represented as mean ± SEM.

(C) Illustration of PSD-95 and its five domains with the sequence of PDZ1 highlighted (sequence from UniProtKB P78352, DLG4_HUMAN). Here, the two phosphorylation sites, Ser78 and Ser116, are illustrated and the GLGF repeat underlined.

than the observed 100-μM binding affinity of PDZ1 WT to the Stg protein ligand (Figures 4B and S5A) and 10-fold higher than PDZ1-2 WT, which bound with an affinity of 12 μM (Figures 4A and 4B). PDZ1 WT bound the Stg protein ligand with very low affinity, and the variant phosphorylated on Ser78 was observed not to bind (Figure S5A). However, phosphorylation of Ser78 in PDZ1-2 and PSD-95 did not result in the same change of binding affinity (Figures 4A and 4B), which can be explained by an earlier finding that the Stg tail does not bind to the canonical target recognition groove of PDZ1 in the Stg/PDZ1-2 or Stg/PSD-95 complexes (Zeng et al., 2019). Furthermore, the binding was then found to be a single site binding. Phosphorylation of Ser116 in both PDZ1-2 and PSD-95 slightly enhanced binding to the Stg protein ligand, seen as change in the binding slope and thereby had the opposite effect as seen for phosphorylation of Ser78 in PDZ1 (Figures 4A, 4B, and S5A). Phosphorylation of Ser73 and Ser142 in PDZ1 enhanced the weak binding to the Stg protein ligand (Figure S5A), and phosphorylation of Ser73 in PDZ1-2 negatively affected binding (Figure S5B). Phosphorylation of Ser73 and Ser142 in PSD-95 did not alter the binding affinity to the Stg protein ligand (Figure S5C).

The effect on ligand binding was also measured by FP using C-terminal TAMRA-labeled peptide ligands, representing different protein interaction partners (Pedersen et al., 2017). A total of five peptide ligands

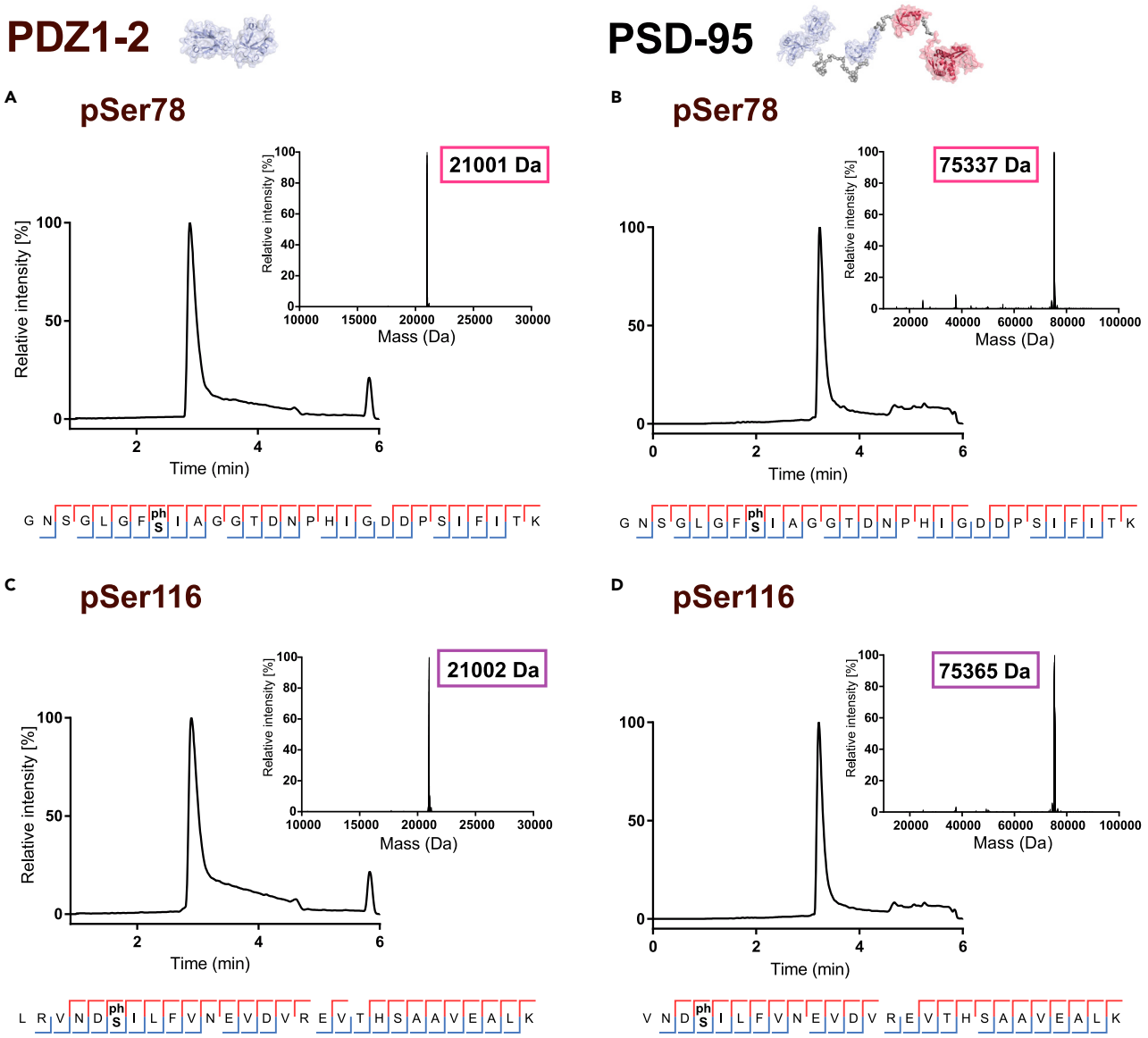

Figure 3. Identification of site-specific phosphorylations

(A) PDZ1-2 pSer78 protein variant. LC-MS spectrum and mass derived from the deconvoluted spectrum of the purified PDZ1-2 pSer78 protein variant. The observed pSer mass is highlighted in color. The expected mass for the PDZ1-2 pSer protein variant was 21,004 Da. Below the spectra is the identified phosphorylated peptide from the LC-MS/MS analysis of the purified protein. The annotated spectrum is found in Figure S3C.

(B) PSD-95 pSer78 protein variant. LC-MS spectrum and mass derived from the deconvoluted spectrum of the purified PSD-95 pSer78 protein variant. The observed pSer mass is highlighted in color. The expected mass for the PSD-95 pSer protein variant was 75,349 Da. Below the spectra is the identified phosphorylated peptide from the LC-MS/MS analysis of the purified protein. The annotated spectrum is found in Figure S4C.

(C) PDZ1-2 pSer116 protein variant. The annotated spectrum is found in Figure S3D.

(D) PSD-95 pSer116 protein variant. The annotated spectrum is found in Figure S4D.

were employed and tested for binding to specific phosphorylated protein variants (Table S3). All proteins bound the peptide ligands with micromolar affinities, and the affinity increased with protein size (Table S4), as was also observed by ITC. PDZ1 WT was observed to bind GluN2B with an affinity of K_d = 12.4 μM; however, phosphorylation of Ser78 disrupted this binding (Figure S6A). Likewise, PDZ1 WT bound to the Stg peptide ligand with an affinity of 27.3 μM, but phosphorylation of Ser78 disrupted this binding (Figure S6A). Phosphorylation of Ser78 in PDZ1-2 and PSD-95 did, however, not display the same dramatic effect on binding to both GluN2B and Stg peptide ligands (Figures 4C and 4D). PDZ1-2 and PSD-95 WT proteins

Table 1. LC-MS/MS derived data values for all protein variants

Protein	Site	Localization probability	Intensity	Score	Delta score
PDZ1	pSer73	0.9991	6.4E+10	253.00	239.41
	pSer78	1	3.2E+10	238.46	225.97
	pSer142	1	1.7 E+10	257.76	240.35
PDZ1-2	pSer73	0.9998	1.5E+10	320.75	306.10
	pSer78	1	1.7E+10	228.38	214.61
	pSer116	1	4.1E+09	196.08	178.01
PSD-95	pSer73	1	1.2E+10	261.51	246.59
	pSer78	1	1.3E+10	229.6	213.36
	pSer116	1	2.8E+10	206.71	189.43
	pSer142	1	1.6E+10	161.55	141.73
	pSer295	NA	NA	NA	NA

For each protein variant of PDZ1, PDZ1-2, and PSD-95, the localization probability, summed intensity, averaged score, and delta score are listed.

bound GluN2B with almost equally high affinities of 1.9 μM and 1.2 μM, respectively, but phosphorylation of Ser78 in both proteins did not affect this binding (Figures 4C and 4D; Table S4). Both PDZ1-2 and PSD-95 WT were also observed to bind the Stg peptide ligand with high affinities of 7.5 μM and 2.7 μM, respectively, and here, phosphorylation of Ser78 negatively affected the binding, however not significantly (Figures 4C and 4D; Table S4). Phosphorylation of Ser116 in PDZ1-2 was observed to slightly enhance binding to the Stg peptide ligand, which was also observed by ITC with the Stg protein ligand (Figure 4C; Table S4). Phosphorylation of Ser116 in PSD-95 slightly decreased binding to the Stg peptide, albeit not significantly (Figure 4D; Table S4). An overall clear tendency was seen, although not observed for all three protein variants (single, tandem, and FL PSD-95) across both assays; namely binding to GluN2B and Stg was affected by phosphorylation of Ser78 and Ser116, negatively and positively, respectively.

Phosphorylation of Ser73 in PDZ1 negatively affected binding to both GluN2A and GluN2B subunits of the NMDA receptor (Figure S6A), as previously observed (Pedersen et al., 2017). The effect was not as significant for phosphorylation of the same site in the tandem or PSD-95 protein variants (Figures S6B and S6C). Phosphorylation of Ser142 in PDZ1 and PSD-95 did not affect binding to the C-terminal peptides representing the Kv1.4 or Kv1.7 potassium channels (Figures S6A and S6C).

Interestingly, increased binding affinities of ligands were observed with an increase in protein size, which could be a result of multiple factors including the multivalent binding nature of the protein in contrast to particularly the single PDZ domain. The PDZ3-SH3-GK module of PSD-95 functions as another binding site for ligands, and in addition, the FL of PSD-95 can experience target-binding-induced multimerization in contrast to single PDZ domains, which could increase the avidity of the binding (Zeng et al., 2018b). Altogether this could lead to weaker phenotypes for the phosphorylated FL PSD-95 protein variants relative to the single domain variants, observed as a less impact of phosphorylation on measured binding affinities.

Effect of phosphorylation on phase separation with GluN2B and stargazin

We have previously shown that the tandem domain of PSD-95 is necessary for the phase separation with Stg protein, as the single domain alone did not phase separate (Zeng et al., 2019). To test if the introduced phosphorylations in PDZ1-2 and PSD-95 also affected the phase separation with both GluN2B and Stg protein ligands, sedimentation-based experiments were used to assess the formation of condensates. The protein ligands were mixed individually with the phosphorylated protein variants and the ratio of protein in the aqueous (supernatant) and condensed (pellet) phases analyzed by gel electrophoresis.

Both PDZ1-2 and PSD-95 were observed to form condensates via LLPS with GluN2B at 10 and 5 μM, respectively (Figures 5A and S6D). Phosphorylation of Ser78 in PDZ1-2 was observed to inhibit phase separation with GluN2B, as less protein was seen in the condensate in comparison to phase separation with the WT protein variant. Interestingly, measured by FP, phosphorylation of Ser78 in PDZ1-2 did not affect binding

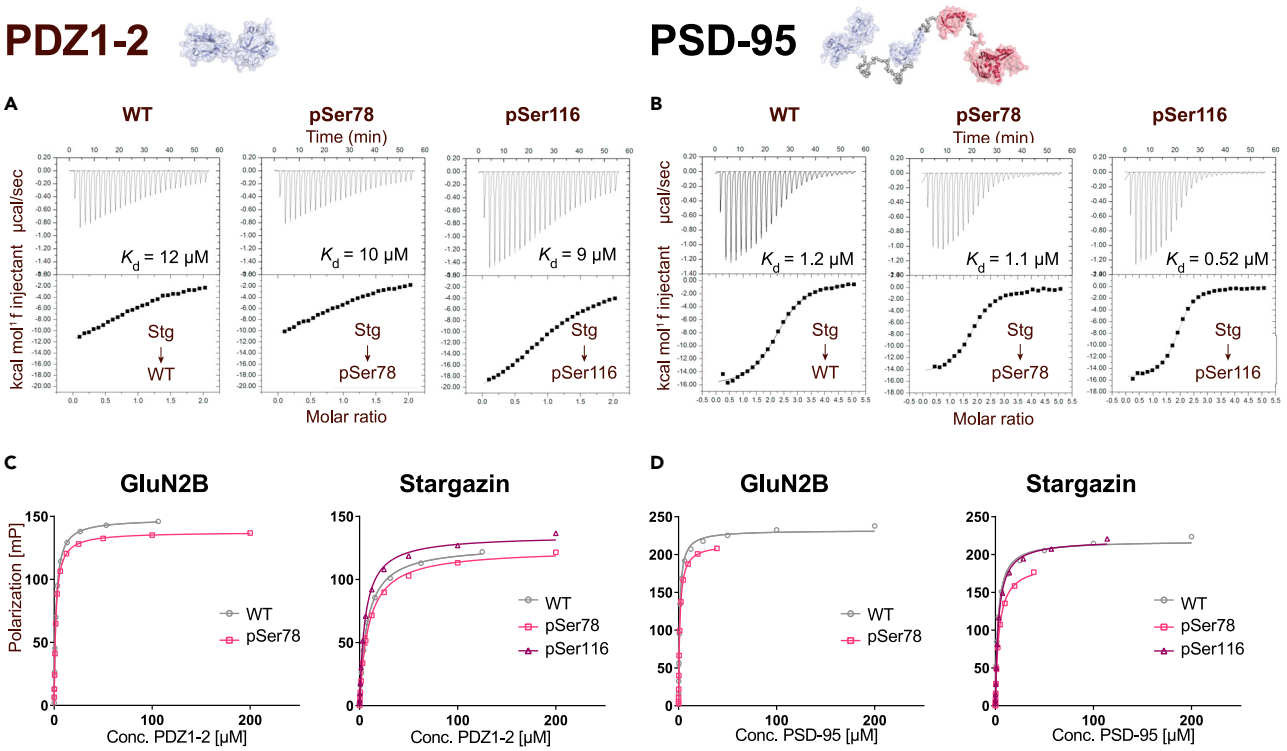

Figure 4. Effect of phosphorylation of Ser78 and Ser116 on binding to stargazin and GluN2B

(A) ITC-based measurements of the PBM and C-terminal of stargazin (Stg) protein binding to PDZ1-2 WT, pSer78, and pSer116. 250-µM Stg was titrated into 25-µM PDZ1-2 in the cell, and binding constants (Kd) were calculated.

(B) ITC-based measurements of the PBM and C-terminal of stargazin (Stg) protein binding to PSD-95 WT, pSer78, and pSer116. 250-µM Stg was titrated into 10-µM PSD-95 in the cell, and binding constants (Kd) were calculated.

(C) PDZ1-2 binding to GluN2B and stargazin peptide ligands measured in a saturation FP assay. Here, 200 nM of the TAMRA-labeled C-terminal peptide ligand was saturated with protein in a concentration-dependent manner with a maximum concentration of 200 µM protein, if possible. The mP was measured for all concentrations in triplicates, background fluorescence subtracted, and the data fitted to a one-sided binding model from which the Kd values were calculated. The Kd values are listed in Table S5 and highlighted Ser78 (*) and Ser116 (*). Data are represented as mean ± SEM.

(D) PSD-95 binding to GluN2B and stargazin peptide ligands measured in a saturation FP assay. The conditions described in (C) were used, and the Kd values are listed in Table S5.

to GluN2B peptide (Figure 4C), but the effect on phase separation with the protein ligand was clearly noticeable. The same inhibitory effect was observed by ITC and FP for PDZ1 pSer78, but as single domains do not phase separate, this was not evaluated. Neither phosphorylation of Ser116 in PDZ1-2 nor phosphorylation of Ser73, Ser142, and Ser295 in PSD-95 had an effect on phase separation with GluN2B (Figures 5A and S6D).

Phase separation of both PDZ1-2 and PSD-95 with Stg protein was also observed (Figures 5A, 5B, and S6E), and phosphorylation of Ser78 in PDZ1-2 also clearly inhibited the formation of condensates with the Stg protein. The effect was less significant for PSD-95 pSer78, but more PSD-95 pSer78 and Stg protein was observed in the aqueous phase, indicating inhibition of condensate formation. On the contrary, phosphorylation of Ser116 in PDZ1-2 promoted phase separation with Stg protein. None of the remaining sites resulted in altered formation of condensates via LLPS; this supports what was also observed by both ITC and FP assays (Figures 4, S5, and S6).

We also observed LLPS of PSD-95 and Stg protein under light microscopy (Figure 5C). Differential interference contrast (DIC) images revealed numerous spherical-shaped and micron-sized droplets of PSD-95 WT and Stg protein, and fluorescence images showed that the droplets were enriched with Stg protein. Ser78 phosphorylation in PSD-95 was observed to inhibit the formation of lipid-droplets, as also seen by sedimentation assays. Phosphorylation of Ser116 was in contrast observed to promote concentration of protein

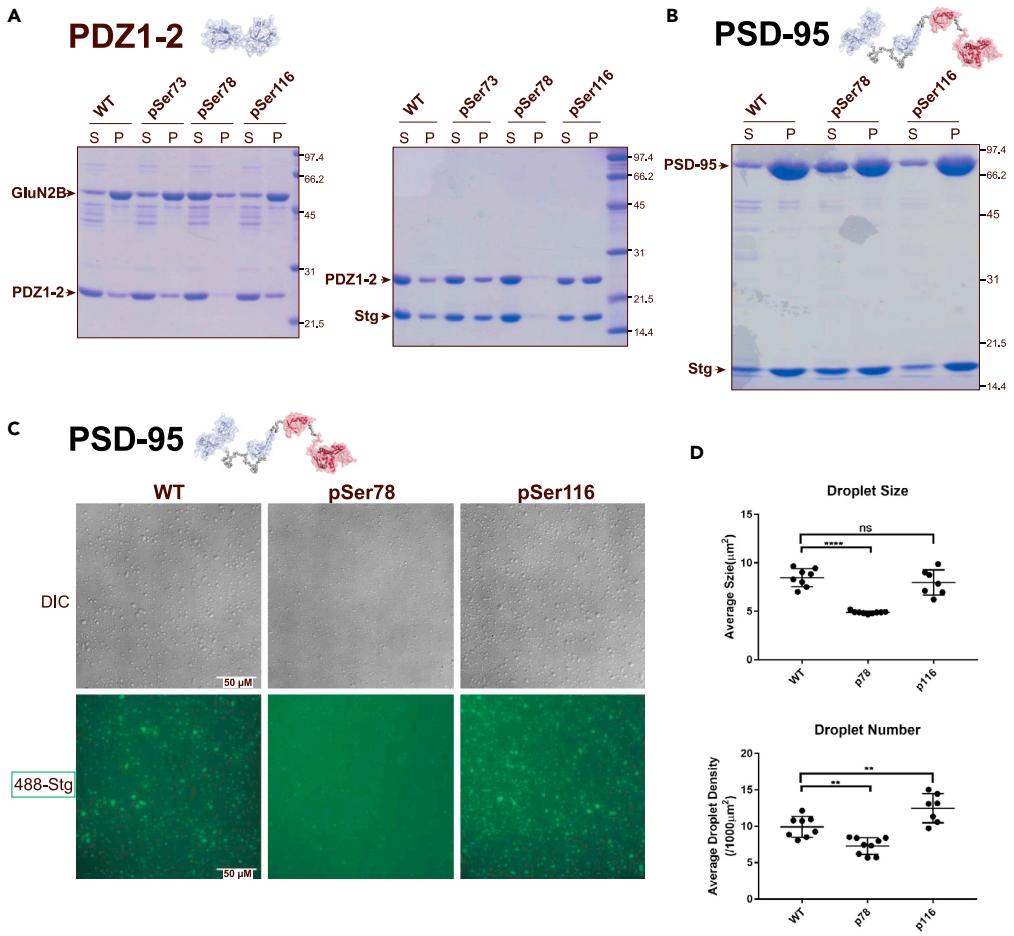

Figure 5. Effect of phosphorylation on phase separation with GluN2B and stargazin

(A) PDZ1-2 (10 μM) was mixed with GluN2B protein (10 μM) (left) and stargazin (Stg) protein (right), equilibrium reached, and the mixture spun down. Hereafter, the supernatant (S) and resuspended pellet (P) was loaded on a gel, which was Coomassie stained to visualize the protein bands. Bands corresponding to PDZ1-2, GluN2B, and Stg are indicated by an arrow. For sedimentation assays with PDZ1-2, 10-μM PDZ1-2 and 10-μM GluN2B were used, and 75 μM PDZ1-2 protein and 75 μM Stg protein ligand.

(B) PSD-95 was mixed with stargazin (Stg) protein, equilibrium reached, and the mixture spun down. Hereafter, the supernatant (S) and resuspended pellet (P) was loaded on a gel, which was Coomassie stained to visualize the protein bands. Bands corresponding to PSD-95 and stargazin are indicated by an arrow. For sedimentation assays with PSD-95, 5-μM pSer78 and pSer116 protein and 12.5-μM Stg protein were used.

(C) DIC (top) and fluorescence (bottom) images showing the phase separation of PSD-95 WT, pSer78, and pSer116 (5 μM) with Stg protein (12.5 μM). For the fluorescence images Stg protein was labeled with Alexa Fluor 488. Scale bar represents 50 μM.

(D) Quantification of imaging data presented in (C); droplet size (top) and Stg protein enrichment in the droplets presented as droplet number (bottom).

in the condensed phase, which was not clearly visible in the sedimentation assays for PSD-95 but is supported by the sedimentation results for PDZ1-2. Quantification done by measuring the average droplet size and number of droplets also showed that the introduced phosphorylations in PSD-95 affected the phase separation with the Stg protein ligand (Figure 5D), with pSer78 negatively affecting both the droplet size and number and pSer116 increasing the droplet number.

DISCUSSION

PSD-95 is one of the most abundant proteins of the PSD and orchestrates signaling of particularly the AMPA and NMDA receptors through interactions finetuned by posttranslational modifications (PTMs), such as phosphorylation. The interactions are primarily mediated by the three PDZ domains of PSD-95,

and due to the multivalent binding mode of PSD-95, the interactions are highly complex. The effect of site-specific phosphorylation on the complex interactions are however largely unknown, and here we aimed to evaluate this by combining biochemical binding assays with phase separation studies of genetically phosphorylated protein variants of PSD-95.

Here, we generated 11 site-specifically Ser phosphorylated protein variants of PSD-95 using amber codon suppression and found that the introduced phosphorylations did not affect the protein fold (Figures 1 and 2A). We have previously site-specifically phosphorylated single PDZ domains of PSD-95 using a semi-synthetic approach (Pedersen et al., 2017) but here Ser residues in the single, tandem, and PSD-95 were phosphorylated in both high yields and purity; this indicated the strength of the approach for generation of many phosphorylated protein variants. With amber codon suppression, theoretically all Ser residues can be phosphorylated (Rogerson et al., 2015), but we observed differential suppression depending on the site of introduction (Figure 1B). Two positions in PDZ1 of the single and tandem protein variants were not successfully suppressed (Ser93 and Ser131), and furthermore, two positions were only successfully phosphorylated in either one of the variants (Ser116 and Ser142). Interestingly, all attempted positions phosphorylated in PDZ1 of PSD-95 were however successfully suppressed. Site-dependable suppression of amber codons is a common challenge in the field of genetic incorporation of nonnatural amino acids and can be the result of various factors (Chin, 2017). The sequence context of the inserted amber codon can affect the suppression efficiency with nucleotides both upstream and downstream of the amber codon potentially limiting the suppression efficiency (Schwark et al., 2018; Xu et al., 2016). The localization of the amber codon within a protein as well as the stability of the expressed protein can furthermore affect the expression of noncanonical amino-acid-containing proteins, affecting the protein yield (Zhu et al., 2019). In contrast to the natural mechanism for post-translational modification of a protein, expression of phosphorylated proteins using amber codon suppression requires the protein to fold with the inserted phosphorylation, which potentially could also affect the expression efficiency. These challenges can be addressed by exploring the usage of other bacterial strains, where e.g., amber stop codons have been recoded and release factor (RF) proteins have been deleted (Heinemann et al., 2012; Lajoie et al., 2013; Mukai et al., 2015), to increase the expression of phosphorylated protein. Many of these strains have however suffered from low fidelity, with a high insertion of canonical amino acids in response to the amber codon, slow growth rates, and an unhealthy metabolism. Various systems have furthermore been developed for pSer insertion in both proteins (Lee et al., 2013; Pirman et al., 2015) and peptides (Barber et al., 2018) and could be evaluated to determine the cause for the differential site suppression seen here; this has been done recently using a further developed pSer system in a healthy RF-deficient strain (Zhu et al., 2019). As we only saw the differential site-dependence for the single and tandem domains, the differential suppression could however indicate that other factors such as stability or functionality of the modified protein affected the outcome. Furthermore, approaches for the genetic introduction of pTyr (Hoppmann et al., 2017; Luo et al., 2017) and pThr (Zhang et al., 2017) have been developed. As PSD-95 is also regulated by phosphorylation of Tyr (Zhang et al., 2011) and Thr (Nelson et al., 2013) residues, evaluating the feasibility of these approaches and their phosphorylation effect could be interesting.

All phosphorylated proteins were purified in high purity, albeit the yields decreased with increased protein size (Figure 1B). The genetic insertion of pSer is a means of competition between the natural translation machinery, reading the amber codon as a stop codon, and the orthogonal, reading the amber codon for pSer insertion, and the expression of truncated protein product is therefore evident as a factor affecting the overall protein yield (Chin, 2017). Expression of truncated product was seen for all sites attempted suppressed in the PSD-95 protein variant, and the expression of truncated protein products were greater for positions 295, 425, and 561. These were therefore either purified in very low yield or not at all. The truncated products of the single and tandem domains were undetectable due to their small size not being visible by SDS-PAGE, and the expression of truncated product could therefore not be evaluated for these protein variants. It is hence unclear if the lower yield of PSD-95 protein in contrast to the single and tandem domains was primarily due to loss of protein during purification or also differential expression efficiency with lower expression of PSD-95 phosphorylated protein. The site-specific phosphorylations were verified using tandem-MS, with all sites showing both high localization probabilities and intensities (Figures 3 and S2–S4; Table 1). The results highly correlated with the expression and purification results, as the PSD-95 pSer295 protein variant, which was insufficiently suppressed, was more difficult to detect by tandem-MS; this suggested that better and more accurate phosphorylation was achieved with high suppression efficiency.

When evaluating the effect of the site-specific phosphorylations by ITC and FP assays, as well as phase separation, a clear tendency was seen (Figures 4 and 5). Here we observed an increased binding affinity for

both peptide and protein ligands with an increase in the size of the protein variants, with highest affinity for PSD-95, then PDZ1-2 and lowest for PDZ1, albeit this was also accompanied by a weaker phenotype of the introduced phosphorylations. PSD-95 protein variants were found to bind ligands, both peptides and proteins, with up to 10-fold higher affinity than PDZ1 variants, but the effect of phosphorylation of the multivalent PSD-95 was less pronounced than phosphorylation of the single PDZ1 domain. Phosphorylation of Ser78 in the PDZ1 protein variant resulted in no binding of Stg or GluN2B ligands, both peptides and proteins. Observed by biochemical binding assays, this effect was less significant for phosphorylation of the same site in both the PDZ1-2 and PSD-95 protein variants. The effect was more pronounced when observed by phase separation, especially for PDZ1-2, where the results also strongly indicated that phosphorylation of Ser116 promoted phase separation with Stg only, functionally contrary to phosphorylation of Ser78. Altogether, the results of the different assays supported each other and showed an interesting differential effect of phosphorylation of Ser78 and Ser116.

The increased binding affinity and less significant effect of phosphorylation of PSD-95 in contrast to PDZ1 could be attributed to the compensatory mechanisms of the additional protein domains as well as the multivalent binding mode of PSD-95 (Zeng et al., 2019). The multimerization capabilities of PSD-95 could likely have contributed to the increased binding affinity that we observed and resulted in the introduced phosphorylations having a minor effect on the interaction with the various binding partners but were however also driving forces for the formation of LLPS condensates. The ability of proteins to phase separate and the threshold for phase separation relies on multiple factors including the domain valency and intrinsically disordered regions in the protein sequence (Banani et al., 2017; Chen et al., 2020; Li et al., 2020). Multivalency drives LLPS and increased network valency tends to enhance phase separation (Li et al., 2012). Despite clear formation of condensates, the lower threshold for phase separation of PDZ1-2 protein variants with the two ligands could therefore explain the very visible effect of phosphorylation. Likewise, the added valency from the additional domains in PSD-95 could explain lack of a clear observable effect of phosphorylation of the multidomain protein.

Previous studies have shown that Stg uses its entire C-terminal (amino acids 203-323) including the PBM to bind to PSD-95 via specific and multivalent interactions, which also governs the phase separation with PSD-95 (Zeng et al., 2019). Namely, the disordered Arg-rich C-terminal has been found to bind PDZ1, and the PBM preferably binds to PDZ2 of PSD-95, with the Arg-rich region being highly important for LLPS. This multivalent nature of the Stg/PSD-95-complex could also explain the less visible effect of Ser78 phosphorylation of both the PDZ1-2 tandem domain and PSD-95 in contrast to phosphorylation of the same position in PDZ1, as the interaction would have an increased affinity and shield the effect of the introduced phosphorylation. This would explain the dramatic effect of phosphorylation of Ser78 in PDZ1 but could be further investigated. Likewise, the interaction between PDZ1 and the Arg-rich C-terminal of Stg is governed by the negatively charged surface of PDZ1 (Zeng et al., 2019), and as Ser116 is near this surface, phosphorylation would increase the negative charges and promote interaction.

Interestingly, our results identify two novel phosphorylation sites in PDZ1 of PSD-95, namely Ser78 and Ser116, with opposing effects on ligand binding and phase separation. Phosphorylation of Ser78 inhibited binding of both GluN2B and Stg, whereas phosphorylation of Ser116 promoted binding with Stg only, which could indicate importance in receptor distribution, removal and accumulation, and thereby synaptic transmission. To verify the possible biological importance, the functionality of these phosphorylations could be further investigated by introducing nonbinding mutations or genetically encoding a nonhydrolyzable analogue for cellular studies.

Overall, the data presented proved the feasibility of amber codon suppression for genetic introduction of site-specific phosphorylations in three different protein variants of PSD-95 and, in combination with both biochemical assays and phase separation, was found to be a good approach for the identification of novel phosphorylations sites.

Limitations of the study

The study demonstrated the genetic introduction of pSer residues into three different protein variants of PSD-95 and, using biochemical assays and phase separation, found two sites to affect the dynamics of the PSD. The production of proteins with genetically introduced pSer residues is difficult and exhibits challenges both on the site level, e.g., the sequence context of the amber codon, and the protein level,

e.g., stability of the expressed protein, potentially resulting in low amounts of purified protein or no yield for some. This is thus a limitation of the project, as additional replications for quantification of some experiments as well as conducting 2D phase diagrams of the phase separation assays were not possible. The presented results show an effect of phosphorylation of Ser78 and Ser116 on the phase separation with GluN2B and Stg, which could be quantified and further explored by cellular assays if more protein was available. Furthermore, the two phosphorylations have not previously been identified, thus warranting further studies, where additional cell-based experiments are performed.

STAR★METHODS

Detailed methods are provided in the online version of this paper and include the following:

- KEY RESOURCES TABLE
- RESOURCE AVAILABILITY
  - Lead contact
  - Materials availability
  - Data and code availability
- METHOD DETAILS
  - Plasmid generation
  - Protein expression incl. double transformation
  - Protein purification
  - Protein validation: LC-MS and UPLC
  - LC-MS/MS
  - Circular dichroism
  - Peptide synthesis
  - Fluorescence polarization
  - Phase transition sedimentation and imaging assay
  - Isothermal titration calorimetry (ITC) assay
- QUANTIFICATION AND STATISTICAL ANALYSIS

SUPPLEMENTAL INFORMATION

Supplemental information can be found online at https://doi.org/10.1016/j.isci.2021.103268.

ACKNOWLEDGMENTS

The work was supported by grants from the Graduate School of Health and Medical Sciences, UCPH and The Center for Biopharmaceuticals, UCPH to KS and grants from Research Grant Council of Hong Kong (AoE-M09-12 and C6004-17G) to MZ. MZ is a Kerry Holdings Professor of Science and a Croucher Foundation Senior Fellow. The construct pKW2 EF-Sep was kindly provided by Professor Jason Chin, Cambridge, UK. Nikolaj Riis Christensen and Mette Ishøy Rosenbaum contributed with scientific guidance and discussion. Parts of the graphical abstract were created with BioRender.com.

AUTHOR CONTRIBUTIONS

MVP, TLJ, and SB expressed and purified the pSer protein variants and characterized the proteins. MVP and SB performed all FP experiments. MVP and SCBL performed LC-MS/MS analysis. CM purified protein for LLPS and XC performed ITC and LLPS experiments. CRB synthesized peptide ligands. MVP, XC, and SCBL analyzed all the data. MVP, XC, LSC, MZ, and KS designed the research. MVP and KS drafted the paper. All authors commented on the paper.

DECLARATION OF INTERESTS

The authors declare no competing interests.

Received: October 8, 2020
Revised: January 11, 2021
Accepted: October 12, 2021
Published: November 19, 2021

REFERENCES

Aarts, M., Liu, Y., Liu, L., Besshoh, S., Arundine, M., Gurd, J.W., Wang, Y.T., Salter, M.W., and Tymianski, M. (2002). Treatment of ischemic brain damage by perturbing NMDA receptor– PSD-95 protein interactions. Science *298*, 846–850.

Bach, A., Clausen, B.H., Moller, M., Vestergaard, B., Chi, C.N., Round, A., Sorensen, P.L., Nissen, K.B., Kastrup, J.S., Gajhede, M., et al. (2012). A high-affinity, dimeric inhibitor of PSD-95 bivalently interacts with PDZ1-2 and protects against ischemic brain damage. Proc. Natl. Acad. Sci. U S A *109*, 3317–3322.

Ballif, B.A., Carey, G.R., Sunyaev, S.R., and Gygi, S.P. (2008). Large-scale identification and evolution indexing of tyrosine phosphorylation sites from murine brain. J. Proteome Res. *7*, 311–318.

Banani, S.F., Lee, H.O., Hyman, A.A., and Rosen, M.K. (2017). Biomolecular condensates: organizers of cellular biochemistry. Nat. Rev. Mol. Cell Biol. *18*, 285–298.

Barber, K.W., Muir, P., Szeligowski, R.V., Rogulina, S., Gerstein, M., Sampson, J.R., Isaacs, F.J., and Rinehart, J. (2018). Encoding human serine phosphopeptides in bacteria for proteome-wide identification of phosphorylation-dependent interactions. Nat. Biotechnol. *36*, 638–644.

Chen, L., Chetkovich, D.M., Petralia, R.S., Sweeney, N.T., Kawasaki, Y., Wenthold, R.J., Bredt, D.S., and Nicoll, R.A. (2000). Stargazin regulates synaptic targeting of AMPA receptors by two distinct mechanisms. Nature *408*, 936–943.

Chen, X., Nelson, C.D., Li, X., Winters, C.A., Azzam, R., Sousa, A.A., Leapman, R.D., Gainer, H., Sheng, M., and Reese, T.S. (2011). PSD-95 is required to sustain the molecular organization of the postsynaptic density. J. Neurosci. *31*, 6329–6338.

Chen, X., Levy, J.M., Hou, A., Winters, C., Azzam, R., Sousa, A.A., Leapman, R.D., Nicoll, R.A., and Reese, T.S. (2015). PSD-95 family MAGUKs are essential for anchoring AMPA and NMDA receptor complexes at the postsynaptic density. Proc. Natl. Acad. Sci. U S A *112*, E6983–E6992.

Chen, X., Wu, X., Wu, H., and Zhang, M. (2020). Phase separation at the synapse. Nat. Neurosci. *23*, 301–310.

Chetkovich, D.M., Chen, L., Stocker, T.J., Nicoll, R.A., and Bredt, D.S. (2002). Phosphorylation of the postsynaptic density-95 (PSD-95)/Discs large/Zona occludens-1 binding site of stargazin regulates binding to PSD-95 and synaptic targeting of AMPA receptors. J. Neurosci. *22*, 5791–5796.

Chi, C.N., Bach, A., Stromgaard, K., Gianni, S., and Jemth, P. (2012). Ligand binding by PDZ domains. Biofactors *38*, 338–348.

Chin, J.W. (2017). Expanding and reprogramming the genetic code. Nature *550*, 53–60.

Coley, A.A., and Gao, W.J. (2018). PSD95: a synaptic protein implicated in schizophrenia or autism? Prog. Neuropsychopharmacol. Biol. Psychiatry *82*, 187–194.

Doyle, D.A., Lee, A., Lewis, J., Kim, E., Sheng, M., and Mackinnon, R. (1996). Crystal structures of a complexed and peptide-free membrane protein–binding domain: molecular basis of peptide recognition by PDZ. Cell *85*, 1067–1076.

Du, C.P., Gao, J., Tai, J.M., Liu, Y., Qi, J., Wang, W., and Hou, X.Y. (2009). Increased tyrosine phosphorylation of PSD-95 by Src family kinases after brain ischaemia. Biochem. J. *417*, 277–285.

El-Husseini, A.E.-D., Schnell, E., Chetkovich, D.M., Nicoll, R.A., and Bredt, D.S. (2000). PSD-95 involvement in maturation of excitatory synapses. Science *290*, 1364–1368.

Feng, W., and Zhang, M. (2009). Organization and dynamics of PDZ-domain-related supramodules in the postsynaptic density. Nat. Rev. Neurosci. *10*, 87–99.

Funke, L., Dakoji, S., and Bredt, D.S. (2005). Membrane-associated guanylate kinases regulate adhesion and plasticity at cell junctions. Annu. Rev. Biochem. *74*, 219–245.

Gardoni, F., Polli, F., Cattabeni, F., and Di Luca, M. (2006). Calcium-calmodulin-dependent protein kinase II phosphorylation modulates PSD-95 binding to NMDA receptors. Eur. J. Neurosci. *24*, 2694–2704.

Gray, E.G. (1959). Axo-somatic and axo-dendritic synapses of the cerebral cortex: an electron microscope study. J. Anat. *93*, 420–433.

Harris, B.Z., Hillier, B.J., and Lim, W.A. (2001). Energetic determinants of internal motif recognition by PDZ domains. Biochemistry *40*, 5921–5930.

Heinemann, I.U., Rovner, A.J., Aerni, H.R., Rogulina, S., Cheng, L., Olds, W., Fischer, J.T., Soll, D., Isaacs, F.J., and Rinehart, J. (2012). Enhanced phosphoserine insertion during Escherichia coli protein synthesis via partial UAG codon reassignment and release factor 1 deletion. FEBS Lett. *586*, 3716–3722.

Hill, M.D., Martin, R.H., Mikulis, D., Wong, J.H., Silver, F.L., Terbrugge, K.G., Milot, G., Clark, W.M., Macdonald, R.L., Kelly, M.E., et al. (2012). Safety and efficacy of NA-1 in patients with iatrogenic stroke after endovascular aneurysm repair (ENACT): a phase 2, randomised, double-blind, placebo-controlled trial. Lancet Neurol. *11*, 942–950.

Hoppmann, C., Wong, A., Yang, B., Li, S., Hunter, T., Shokat, K.M., and Wang, L. (2017). Site-specific incorporation of phosphotyrosine using an expanded genetic code. Nat. Chem. Biol. *13*, 842–844.

Hyman, A.A., Weber, C.A., and Julicher, F. (2014). Liquid-liquid phase separation in biology. Annu. Rev. Cell Dev. Biol. *30*, 39–58.

Kim, E., and Sheng, M. (2004). PDZ domain proteins of synapses. Nat. Rev. Neurosci. *5*, 771–781.

Kim, E., Niethammer, M., Rothschild, A., Jan, Y.N., and Sheng, M. (1995). Clustering of Shaker-type K+ channels by interaction with a family of membrane· associated guanylate kinases. Nature *378*, 85–88.

Kornau, H.-C., Schenker, L.T., Kennedy, M.B., and Seeburg, P.H. (1995). Domain interaction between NMDA receptor subunits and the postsynaptic DensityProtein PSD-95. Science *269*, 1737–1740.

Lajoie, M.J., Rovner, A.J., Goodman, D.B., Aerni, H.R., Haimovich, A.D., Kuznetsov, G., Mercer, J.A., Wang, H.H., Carr, P.A., Mosberg, J.A., et al. (2013). Genomically recoded organisms expand biological functions. Science *342*, 357–360.

Lee, H.J., and Zheng, J.J. (2010). PDZ domains and their binding partners: structure, specificity, and modification. Cell Commun. Signal. *8*, 8.

Lee, S., Oh, S., Yang, A., Kim, J., Soll, D., Lee, D., and Park, H.S. (2013). A facile strategy for selective incorporation of phosphoserine into histones. Angew. Chem. Int. Ed. Engl. *52*, 5771–5775.

Li, P., Banjade, S., Cheng, H.C., Kim, S., Chen, B., Guo, L., Llaguno, M., Hollingsworth, J.V., King, D.S., Banani, S.F., et al. (2012). Phase transitions in the assembly of multivalent signalling proteins. Nature *483*, 336–340.

Li, Q., Peng, X., Li, Y., Tang, W., Zhu, J., Huang, J., Qi, Y., and Zhang, Z. (2020). LLPSDB: a database of proteins undergoing liquid-liquid phase separation in vitro. Nucleic Acids Res. *48*, D320–D327.

Luo, X., Fu, G., Wang, R.E., Zhu, X., Zambaldo, C., Liu, R., Liu, T., Lyu, X., Du, J., Xuan, W., et al. (2017). Genetically encoding phosphotyrosine and its nonhydrolyzable analog in bacteria. Nat. Chem. Biol. *13*, 845–849.

McGee, A.W., Dakoji, S.R., Olsen, O., Bredt, D.S., Lim, W.A., and Prehoda, K.E. (2001). Structure of the SH3-guanylate kinase module from PSD-95 suggests a mechanism for regulated assembly of MAGUK scaffolding proteins. Mol. Cell *8*, 1291–1301.

Morabito, M.A., Sheng, M., and Tsai, L.H. (2004). Cyclin-dependent kinase 5 phosphorylates the N-terminal domain of the postsynaptic density protein PSD-95 in neurons. J. Neurosci. *24*, 865–876.

Mukai, T., Hoshi, H., Ohtake, K., Takahashi, M., Yamaguchi, A., Hayashi, A., Yokoyama, S., and Sakamoto, K. (2015). Highly reproductive Escherichia coli cells with no specific assignment to the UAG codon. Sci. Rep. *5*, 9699.

Nelson, C.D., Kim, M.J., Hsin, H., Chen, Y., and Sheng, M. (2013). Phosphorylation of threonine-19 of PSD-95 by GSK-3beta is required for PSD-95 mobilization and long-term depression. J. Neurosci. *33*, 12122–12135.

Nicoll, R.A., Tomita, S., and Bredt, D.S. (2006). Auxiliary subunits assist AMPA-type glutamate receptors. Science *311*, 1253.

Niethammer, M., Kim, E., and Sheng, M. (1996). Interaction between the C terminus of NMDA receptor subunits and multiple members of the PSD-95 family of membrane-associated guanylate kinases. J. Neurosci. *16*, 2157–2163.

Nishiyama, J., and Yasuda, R. (2015). Biochemical computation for spine structural plasticity. Neuron *87*, 63–75.

Park, H.S., Hohn, M.J., Umehara, T., Guo, L.T., Osborne, E.M., Benner, J., Noren, C.J., Söll, D., and Rinehart, J. (2011). Expanding the genetic code of Escherichia coli with phosphoserine. Science *33*, 1151–1154.

Pedersen, S.W., Pedersen, S.B., Anker, L., Hultqvist, G., Kristensen, A.S., Jemth, P., and Stromgaard, K. (2014). Probing backbone hydrogen bonding in PDZ/ligand interactions by protein amide-to-ester mutations. Nat. Commun. *5*, 3215.

Pedersen, S.W., Albertsen, L., Moran, G.E., Levesque, B., Pedersen, S.B., Bartels, L., Wapenaar, H., Ye, F., Zhang, M., Bowen, M.E., and Stromgaard, K. (2017). Site-specific phosphorylation of PSD-95 PDZ domains reveals fine-tuned regulation of protein-protein interactions. ACS Chem. Biol. *12*, 2313–2323.

Pirman, N.L., Barber, K.W., Aerni, H.R., Ma, N.J., Haimovich, A.D., Rogulina, S., Isaacs, F.J., and Rinehart, J. (2015). A flexible codon in genomically recoded Escherichia coli permits programmable protein phosphorylation. Nat. Commun. *6*, 8130.

Rao, A., Kim, E., Sheng, M., and Craig, A.M. (1998). Heterogeneity in the molecular composition of excitatory postsynaptic sites during development of hippocampal neurons in culture. J. Neurosci. *18*, 1217–1229.

Rappsilber, J., Ishihama, Y., and Mann, M. (2003). Stop and go extraction tips for matrix-assisted laser desorption/ionization, nanoelectrospray, and LC/MS sample pretreatment in proteomics. Anal. Chem. *75*, 663–670.

Rogerson, D.T., Sachdeva, A., Wang, K., Haq, T., Kazlauskaite, A., Hancock, S.M., Huguenin-Dezot, N., Muqit, M.M., Fry, A.M., Bayliss, R., and Chin, J.W. (2015). Efficient genetic encoding of phosphoserine and its nonhydrolyzable analog. Nat. Chem. Biol. *11*, 496–503.

Sainlos, M., Tigaret, C., Poujol, C., Olivier, N.B., Bard, L., Breillat, C., Thiolon, K., Choquet, D., and Imperiali, B. (2011). Biomimetic divalent ligands for the acute disruption of synaptic AMPAR stabilization. Nat. Chem. Biol. *7*, 81–91.

Sattler, R., Xiong, Z., Lu, W.Y., Hafner, M., Macdonald, J.F., and Tymiansky, M. (1999). Specific coupling of NMDA receptor activation to nitric oxide neurotoxicity by PSD-95 protein. Science *284*, 1845–1848.

Schwark, D.G., Schmitt, M.A., and Fisk, J.D. (2018). Dissecting the contribution of release factor interactions to amber stop codon reassignment efficiencies of the methanocaldococcus jannaschii orthogonal pair. Genes (Basel) *9*, 546.

Sheng, M., and Hoogenraad, C.C. (2007). The postsynaptic architecture of excitatory synapses: a more quantitative view. Annu. Rev. Biochem. *76*, 823–847.

Sheng, M., and Kim, E. (2011). The postsynaptic organization of synapses. Cold Spring Harb. Perspect. Biol. *3*, a005678.

Vallejo, D., Codocedo, J.F., and Inestrosa, N.C. (2016). Posttranslational modifications regulate the postsynaptic localization of PSD-95. Mol. Neurobiol. *54*, 1759–1776.

Volk, L., Chiu, S.L., Sharma, K., and Huganir, R.L. (2015). Glutamate synapses in human cognitive disorders. Annu. Rev. Neurosci. *38*, 127–149.

Witte, M.D., Theile, C.S., Wu, T., Guimaraes, C.P., Blom, A.E., and Ploegh, H.L. (2013). Production of unnaturally linked chimeric proteins using a combination of sortase-catalyzed transpeptidation and click chemistry. Nat. Protoc. *8*, 1808–1819.

Xie, J., and Schultz, P.G. (2005). An expanding genetic code. Methods *36*, 227–238.

Xu, H., Wang, Y., Lu, J., Zhang, B., Zhang, Z., Si, L., Wu, L., Yao, T., Zhang, C., Xiao, S., et al. (2016). Re-exploration of the codon context effect on amber codon-guided incorporation of noncanonical amino acids inEscherichia coliby the blue-White screening assay. Chembiochem *17*, 1250–1256.

Xue, Y., Ren, J., Gao, X., Jin, C., Wen, L., and Yao, X. (2008). GPS 2.0, a tool to predict kinase-specific phosphorylation sites in hierarchy. Mol. Cell. Proteomics *7*, 1598–1608.

Ye, F., and Zhang, M. (2013). Structures and target recognition modes of PDZ domains: recurring themes and emerging pictures. Biochem. J. *455*, 1–14.

Zeng, M., Shang, Y., Araki, Y., Guo, T., Huganir, R.L., and Zhang, M. (2016). Phase transition in postsynaptic densities underlies formation of synaptic complexes and synaptic plasticity. Cell *166*, 1163–1175.e12.

Zeng, M., Chen, X., Guan, D., Xu, J., Wu, H., Tong, P., and Zhang, M. (2018a). Reconstituted postsynaptic density as a molecular platform for understanding synapse formation and plasticity. Cell *174*, 1172–1187.e16.

Zeng, M., Ye, F., Xu, J., and Zhang, M. (2018b). PDZ ligand binding-induced conformational coupling of the PDZ-SH3-GK tandems in PSD-95 family MAGUKs. J. Mol. Biol. *430*, 69–86.

Zeng, M., Diaz-Alonso, J., Ye, F., Chen, X., Xu, J., Ji, Z., Nicoll, R.A., and Zhang, M. (2019). Phase separation-mediated TARP/MAGUK complex condensation and AMPA receptor synaptic transmission. Neuron *104*, 529–543 e6.

Zhang, J., Petit, C.M., King, D.S., and Lee, A.L. (2011). Phosphorylation of a PDZ domain extension modulates binding affinity and interdomain interactions in postsynaptic density-95 (PSD-95) protein, a membrane-associated guanylate kinase (MAGUK). J. Biol. Chem. *286*, 41776–41785.

Zhang, M.S., Brunner, S.F., Huguenin-Dezot, N., Liang, A.D., Schmied, W.H., Rogerson, D.T., and Chin, J.W. (2017). Biosynthesis and genetic encoding of phosphothreonine through parallel selection and deep sequencing. Nat. Methods *14*, 729–736.

Zhu, J., Shang, Y., and Zhang, M. (2016). Mechanistic basis of MAGUK-organized complexes in synaptic development and signalling. Nat. Rev. Neurosci. *17*, 209–223.

Zhu, P., Gafken, P.R., Mehl, R.A., and Cooley, R.B. (2019). A highly versatile expression system for the production of multiply phosphorylated proteins. ACS Chem. Biol. *14*, 1564–1572.

STAR★METHODS

KEY RESOURCES TABLE

REAGENT or RESOURCE	SOURCE	IDENTIFIER
Bacterial and virus strains		
E.coli BL21 competent cells (DE3, pLysS)	Invitrogen	#C606003
E.coli BL21ΔSerB cells	Addgene	#34929
E.coli BL21 cells	Invitrogen	#C600003
Chemicals, peptides, and recombinant proteins		
Isopropyl β-D-1-thiogalactopyranoside (IPTG)	VWR	#437145X
O-phospho-L-serine	Sigma	#P0878
Recombinant protein: PDZ1 6xHis and mutants (pSer73, pSer78, pSer142)	This paper	N/A
Recombinant protein: PDZ1-2 6xHis and mutants (pSer73, pSer78, pSer116)	This paper	N/A
Recombinant protein: PSD-95 6xHis and mutants (pSer73, pSer78, pSer116, pSer142, pSer295)	This paper	N/A
Recombinant protein: Stg CT WT	(Zeng et al., 2019)	N/A
Recombinant protein: GluN2B WT	This paper	N/A
AVLX-144	(Bach et al., 2012)	N/A
Peptide ligand: GluN2A (TAMRA-NNG-KKMPSIESDV)	(Pedersen et al., 2017)	N/A
Peptide ligand: GluN2B (TAMRA-NNG-YEKLSSIESDV)	(Pedersen et al., 2017)	N/A
Peptide ligand: Stargazin (TAMRA-NNG-NTANRRTTPV)	(Pedersen et al., 2017)	N/A
Peptide ligand: Kv1.4 (TAMRA-NNG-SNAKAVETDV)	(Pedersen et al., 2017)	N/A
Peptide ligand: Kv1.7 (TAMRA-NNG-PAGKHMVTEV)	(Pedersen et al., 2017)	N/A
Alexa fluor 488 succinimidyl ester	ThermoFisher	#A20000
Lysyl endopeptidase (Lys-C)	Wako Chemicals	#129-02541
Trypsin, proteomics grade	Sigma Aldrich	#T6567
Deposited data		
PDZ1-2 (PDB: 3GSL)	(Sainlos et al., 2011)	3GSL
PDZ3 (PDB: 5JXB)	(Zeng et al., 2016)	5JXB
SH3-GK (PDB: 1KJW)	(McGee et al., 2001)	1KJW
Recombinant DNA		
Plasmid: pCDF-1b PSD-95 PDZ1 6xHis and mutants (Ser73TAG, Ser78TAG, Ser93TAG, Ser116TAG, Ser131TAG, Ser142TAG)	This paper	N/A
Plasmid: pCDF-1b PSD-95 PDZ1-2 6xHis and mutants (Ser73TAG, Ser78TAG, Ser93TAG, Ser116TAG, Ser131TAG, Ser142TAG, Ser173TAG, Ser217TAG)	This paper	N/A
Plasmid: pCDF-1b Trx HRV 3C PSD-95 61-724 6xHis and mutants (Ser73TAG, Ser78TAG, Ser116TAG, Ser142TAG, Ser295TAG, Ser425TAG, Ser561TAG)	This paper	N/A
Plasmid: Trx 6xHis HRV 3C mouse Stg CT WT 203-323	(Zeng et al., 2019)	N/A
Plasmid: GB1 6xHis HRV 3C rat GluN2B WT 1170-1482	This paper	N/A
Software and algorithms		
Prism	GraphPad	https://www.graphpad.com/scientific-software/prism/
ImageJ	NIH	https://imagej.nih.gov/ij/
MaxQuant software	version 1.5.3.30	

RESOURCE AVAILABILITY

Lead contact

Further information and requests for resources should be directed to and will be fulfilled by the lead contact, Dr. Kristian Strømgaard (kristian.stromgaard@sund.ku.dk).

Materials availability

This study did not generate any new unique reagents. Requests for the pKW2 EF-Sep construct should be directed to the laboratory of Professor Jason Chin.

Data and code availability

- The data reported in this study is available upon request from the lead contact, Dr. Kristian Strømgaard (kristian.stromgaard@sund.ku.dk).
- This paper does not report original code.
- Any additional information required to reanalyze the data reported in this paper is available from the lead contact upon request.

METHOD DETAILS

Plasmid generation

Three different variants of the human PSD-95 protein were used in this study, PSD-95 61-724, PSD-95 PDZ1 and PSD-95 PDZ1-2. All proteins were expressed with a C-terminal poly-histidine tag (6xHis) from a pCDF-1b vector (Novagen) with spectinomycin resistance and under the control of a T7 lac promoter. The DNA constructs were verified by DNA sequencing (Eurofins Genomics).

To generate pCDF-1b Trx HRV 3C PSD-95 61-724 6xHis, termed PSD-95, the protein coding sequence of PSD-95 61-724 6xHis flanked N-terminally by an overhang, *NdeI* restriction site and a HRV 3C cleavage site, and C-terminally by an *AvrII* restriction site and overhang, was purchased (ThermoFisher Scientific). The recipient vector-construct, pCDF-1b Trx *NdeI* HRV 3C PSD-95 1-724 6xHis *AvrII*, which was available in the laboratory, and the purchased sequence were digested with *NdeI* and *AvrII* restriction enzymes overnight (ON) at 37°C. The recipient vector and protein coding sequence were purified using a NucleoSpin® Gel and PCR Clean-up kit (Macherey-Nagel) and ligated together with a Rapid DNA ligation kit (Roche) in a ratio of 50 ng vector to 150 ng DNA to yield pCDF-1b Trx HRV 3C PSD-95 61-724 6xHis.

The pCDF-1b PSD-95 PDZ1 6xHis construct was generated from the previously described pRSET vector containing the recombinant fragment of PSD-95 PDZ1 flanked N-terminally by a 6xHis (Pedersen et al., 2017). By polymerase chain reaction (PCR) amplification, the N-terminal 6xHis tag was removed and replaced with an *NcoI* restriction site with primer MVM_034 (Table S1), and a C-terminal 6xHis tag followed by an *AvrII* restriction site was inserted with primer MVM_035 (Table S1). The PCR product was purified using a NucleoSpin® Gel and PCR Clean-up kit (Macherey-Nagel). The purified DNA and the recipient vector pCDF-1b Trx HRV 3C PSD-95 61-724 6xHis were cleaved during enzymatic digest with *NcoI* and *AvrII* ON at 37°C, purified and ligated together to generate pCDF-1b PSD-95 PDZ1 6xHis.

To generate pCDF-1b PSD-95 PDZ1-2 6xHis, the protein coding sequence of PSD-95 PDZ1-2 6xHis flanked N-terminally by an *NcoI* site and C-terminally by an *AvrII* site was purchased. The DNA and the recipient vector pCDF-1b Trx HRV 3C PSD-95 61-724 6xHis were cleaved during enzymatic digest with *NcoI* and *AvrII* ON at 37°C, purified and ligated together to generate pCDF-1b PSD-95 PDZ1-2 6xHis.

Generation of site-mutated serine residues in all constructs were conducted by quick-change PCR followed by *DpnI* digest at 37°C for 1.5 hours (hrs) (New England Biolabs). Forward and reverse primers were designed for each mutated serine position to incorporate a TAG codon instead (Table S1).

Constructs containing the protein coding sequences of stargazin and GluN2B for phase separation studies were generated using standard PCR-based methods, cloned into vector containing an N-terminal Trx-6xHis- to stargazin and GB1-6xHis- to GluN2B followed by an HRV 3C cutting site. Constructs were confirmed by DNA sequencing.

Protein expression incl. double transformation

For the overexpression of all three wild-type (WT) protein variants, *E.coli* BL21 competent cells (DE3, pLysS, Invitrogen) were transformed with pCDF-1b Trx HRV 3C PSD-95 61-724 6xHis, pCDF-1b PSD-95 PDZ1 6xHis and pCDF-1b PSD-95 PDZ1-2 6xHis, respectively, and grown on spectinomycin (100 μg/mL) containing Luria-Bertani (LB) agar-plates ON at 37°C. Single colonies were used to inoculate 100 mL LB media containing antibiotic and pre-cultures were grown ON at 30°C shaking at 210 rpm. Pre-heated LB-media containing antibiotic was inoculated with the overnight cultures to reach an optical density (OD) at 600 nm of 0.1, and expression cultures were grown at 37°C to an OD of 0.4-0.6 before induced with a final concentration of 0.1 mM Isopropyl β-D-1-thiogalactopyranoside (IPTG). PSD-95 was overexpressed for 4 hrs at 30°C, PSD-95 PDZ1 for 4 hrs at 37°C, and PSD-95 PDZ1-2 ON at 18°C. Cells were harvested by centrifugation at 10,000xG, 4°C, 10 min (Sorvall Lynx 6000, Thermo Scientific) and the pellets were stored at −20°C until further use.

For the overexpression of phosphoserine (pSer) variants of all three proteins, *E.coli* BL21Δ*SerB* cells (Addgene #34929) were co-transformed with serine-mutated DNA and the high-copy number pKW2 EF-Sep plasmid kindly provided by Professor Jason Chin, Cambridge, and previously described in (Rogerson et al., 2015). Double transformed bacteria were grown on LB agar-plates containing both spectinomycin (100 μg/mL) and chloramphenicol (25 μg/mL). Overexpression was carried out similarly to overexpression of WT protein, but protein expression was induced with a final concentration of 0.5 mM IPTG and media supplemented O-phospho-L-serine (Sigma) to a final concentration of 1 mM.

E.coli BL21 cells transformed with mouse Stargazin_CT (aa 203-323) fused to the C-terminal end of the Trx-His6-tag or rat GluN2B cytoplasmic tail (aa 1170-1482) fused to the C-terminal end of the GB1-His6-tag were cultured in LB medium at 37°C till OD600 reached 0.8-1.0. IPTG at 0.25 mM final concentration was added to induce protein expression. Stargazin_CT was expressed at 37°C for 2-3 hours, and GluN2B fragment was expressed at 16°C for 16-20 hours.

Protein purification

Protein pellets were lysed in ice-cold lysis buffer, either B-PER™ Bacterial Protein Extraction Reagent (ThermoFisher Scientific) or 50 mM sodium phosphate (NaPi), 10 mM $MgCl_2$, pH 7.4, both supplemented 25 μg/mL DNase and cOmplete protase inhibitor tablets (Roche). If lysed in 50 mM NaPi buffer, lysate was processed in a cell-disrupter apparatus (Constant System Ltd) at 26 kPsi. Hereafter, lysate was spun down by centrifugation at 30,000xG, 4°C, 30 min, and the pH of the supernatant adjusted to 7.5 prior to filtration through a 0.45 μM filter. Protein solutions were loaded on pre-equilibrated HisTrap columns (GE Healthcare) using either a peristaltic pump or an AKTA Start system (GE Healthcare), and eluted with imidazole either isocradically using a peristaltic pump or with a gradient on an AKTA Explorer 100 Air (GE Healthcare) or AKTA Start System (GE Healthcare).

For the purification of PSD-95 6xHis, affinity purification was carried out in 25 mM HEPES, 150 mM NaCl, pH 8, 2 mM BME supplemented either 25 mM imidazole for binding or 250 mM for elution. The purest fractions were pooled and imidazole was removed by dialysis at 4°C ON into 25 mM HEPES, 150 mM NaCl, pH 8, 2 mM BME. Hereafter, the Trx solubility tag was cleaved off with HRV 3C protease (ThermoScientific) during dialysis at 4°C ON into 25 mM HEPES, 10 mM NaCl, pH 8, 2 mM BME before impurities were removed by anion exchange on a MonoQ column, yielding PSD-95 6xHis. For the purification of PSD-95 pSer561, an additional step of size-exclusion chromatography (SEC) (HiLoad Superdex 16/600 200 pg column) was carried out in 25 mM HEPES, 500 mM NaCl, pH 7.4.

For the purification of PSD-95 PDZ1 6xHis and PSD-95 PDZ1-2 6xHis, affinity purification was carried out in 50 mM Tris, 150 mM NaCl, pH 7.4, 2 mM BME supplemented either 25 mM imidazole for binding or 250 mM for elution. The purest fractions were pooled and impurities removed by size-exclusion chromatography (HiLoad Superdex 16/600 75 pg column) in 50 mM Tris, 150 mM NaCl, pH 7.4, 2 mM BME, yielding PSD-95 PDZ1 6xHis and PSD-95 PDZ1-2 6xHis.

Before further experiments, purified protein was dialyzed ON at 4°C into 25 mM HEPES, 150 mM NaCl, pH 8, 2 mM BME.

Purification was followed by validating eluted fractions by sodium dodecyl sulfate polyacrylamide gel electrophoresis (SDS-PAGE) and liquid chromatography-mass spectrometry (LC-MS) (see section for

protein validation), and the purest fractions were pooled and up-concentrated in Amicon-Ultra centrifugal filters (Sigma-Aldrich).

The final purified protein variants were evaluated by LC-MS and reverse phase ultra-performance liquid chromatography (RP-UPLC) (see section for protein validation). The protein concentration was determined using absorbance at λ280 nm measured on a NanoDrop 1000 spectrometer (Thermo Fisher Scientific). The protein yield was calculated based on protein concentration (mg/mL), the end-volume of purified protein, the purity and the volume of expressed cell culture, resulting in a protein yield in mg/L culture.

Recombinant Trx-His6-Stargazin_CT were freshly purified using a nickel-NTA agarose affinity column followed by a size-exclusion chromatography (Superdex 75 from the GE Healthcare) with a column buffer containing 50 mM Tris, pH 7.8, 300 mM NaCl, 1 mM EDTA, 1 mM DTT. The N-terminal Trx-His6-tag was cleaved by HRV 3C protease and removed by an additional step of ion exchange chromatography (Recourse S, GE Healthcare). Finally, a desalting column was used to exchange the protein into the buffer containing 50 mM Tris pH 7.8, 100 mM NaCl, 1 mM EDTA, 1 mM DTT.

GB1-His6-GluN2B(1170-1482) was purified with nickel-NTA agarose affinity column followed by size-exclusion chromatography using Superdex 200 (GE Healthcare) in a buffer containing 50 mM Tris pH 7.8, 300 mM NaCl, 1 mM EDTA, 1 mM DTT. The GB1-His6-tag was cleaved by HRV 3C protease and removed by another step of Superdex 200 size-exclusion chromatography using the same column buffer.

Protein validation: LC-MS and UPLC

Protein concentrations were measured on a Nanodrop 1000 (Thermo Fisher Scientific) and all mass determinations were conducted on an electron spray ionization (ESI) liquid chromatography mass spectrometer (LC-MS) coupled to an Agilent 6410 triple quadrupole with two reverse phase C18 columns (Zorbax Eclipse XBD-C18, 4.6 × 50 mm) and (Agilent, Poroshell, 300SB-C18, 2.1 × 75 mm) for peptide and proteins respectively, using a binary buffer system consisting of H_2O, Acetonitril (MeCN) and formic acid (buffer A: 95:5:0.1; buffer B: 5:95:0.1) at 0.75 mL/min. LC-MS samples were analyzed using the Agilent MassHunter version B.01.03 software. An analytical RP-UPLC (Waters Acquity) system with a reverse phase C18 column for peptides (Acquity UPLC BEH C18, 1.7 μm 2.1 × 50 mm) and C8 column for proteins (Acquity UPLC BEH C8, 1.7 μM 2.1 × 50 mm) using a binary buffer system consisting of H2O, MeCN, trifluoroacetic acid (TFA) (buffer A: 95:5:0.1; buffer B: 5:95:0.1) was used to determine peptide and protein purity at 214 nm.

All samples for LC-MS and UPLC were diluted in buffer A (H_2O, MeCN, TFA (95:5:0.1)) and a maximum of 2 μg protein was loaded.

LC-MS/MS

Sample preparation. For the identification of site-specific serine phosphorylations, approximately 50 μg of protein in 50 mM NaPi pH 8 was subjected to sample preparation for LC-MS/MS analysis. Prior to reduction, PDZ1 pSer142 was denatured in 8M/2M Urea/Thiourea as the only sample. Hereafter, protein disulphides were reduced with 1 mM dithiothreitol (DTT) and free cysteine thiols alkylated with 5.5 mM chloroacetamide (CAA) for 60 min at room temperature (RT). Protein was pre-digested with 1 μg LysC per 100 μg protein for 3-4 hrs shaking at RT, LysC cleaving on the carboxyl side of lysine residues. Protein solutions were diluted in 50 mM ammonium bicarbonate (ABC) pH 8 and depending on the specific phosphorylation site, the protein solutions were either incubated ON at RT shaking with trypsin, cleaving on the carboxyl side of arginine and lysine residues, or LysC, using 1 μg enzyme per 100 μg protein of both enzymes. Hereafter, peptides were acidified to pH 2.5 with trifluoroacetic acid (TFA) and spun down for 50 min at 4700 rpm. Peptides were loaded onto StageTips, 4xC18 microcolumns (Empore Disk C18) (Rappsilber et al., 2003). The C18 StageTips were activated, washed and equilibrated in methanol, 80% acetonitrile in 0.1% formic acid (FA) and 0.1% FA, respectively, before peptide loading. After peptide loading, the StageTips were washed in 0.1% FA, spun dry and peptides directly eluted in 40% acetonitrile in 0.1% FA. Acetonitrile was evaporated by vacuum centrifugation and peptides dissolved in 13 μL 0.1% FA and diluted 1:500 before mass spectrometric analysis.

Mass spectrometry analysis. Samples were analyzed using an EASY-nLC 1200 UHPLC system (Thermo Fisher Scientific) coupled to a Q Exactive HF-X mass spectrometer (Thermo Fisher Scientific). Separation of peptides was performed on a 15 cm analytical column with an inner diameter of 75 μm, packed in-house

using ReproSil-Pur 120 C18-AQ 1.9 μm beads (Dr. Maisch). The analytical column was heated to 40°C, and elution of peptides from the column was achieved by application of gradients with Buffer A (0.1% formic acid) and increasing amounts of Buffer B (80 % acetonitrile in 0.1% formic acid) at a flow rate of 250 nL/min. The primary gradient ranged from 5% Buffer B to 45% Buffer B over 30 min. followed by a wash block and equilibration. Electrospray ionization was achieved using a Nanospray Flex Ion Source (Thermo Fisher Scientific). Spray voltage was set to 2 kV, capillary temperature to 275°C, and RF level to 40%. Full scans were performed at a resolution of 60,000, a maximum injection time of 45 ms, with a scan range of 300 to 1,750 *m/z*, and an automatic gain control (AGC) target of 3×10^6 charges. Precursors were isolated with a width of 1.3 *m/z*, with an AGC target of 2×10^5 charges, and precursor fragmentation was accomplished using higher-energy collisional dissociation (HCD), with normalized collision energy of 28. Fragment scans were performed at a resolution of 60,000, a maximum injection time of 120 ms, a loop count of 7, and a scan range of 200 to 2,000 *m/z*. Selected precursors were excluded from repeated sequencing by setting a dynamic exclusion of 30 s.

Data analysis. All RAW files were analyzed using MaxQuant software (version 1.5.3.30). Default settings were used except as outlined below. For generation of the theoretical spectral library, a HUMAN.fasta database was extracted from UniProt on the 24th of May, 2019. N-terminal acetylation, methionine oxidation, and phosphorylation (S, T, and Y) were set as variable modifications, and cysteine carbamidomethylation as a fixed modification. A maximum allowance of 5 variable modifications per peptide was used, and up to 5 missed cleavages was allowed. Mass tolerance for precursors was set to 20 ppm in the first MS/MS search and 4.5 ppm in the main MS/MS search after mass recalibration. For fragment masses, a tolerance of 20 ppm was used. Data was automatically filtered to achieve a false discovery rate of 1% (default) at the peptide-spectrum match, the protein assignment, and the site-specific level. The evidence file from MaxQuant was filtered, and sorted based on raw-files and modified sequence, to only include identifications with MULTI-MSMS, a localization probability >0.99, a Score >100, and a Delta score >100 (Data S1). The intensities and scores for the identifications presented in Table 1 were summed and averaged, respectively.

Circular dichroism

Circular dichroism (CD) experiments were made on a Jasco J-1500 spectrophotometer with a peltier controlled temperature. Prior to CD measurements, proteins were dialyzed ON at 4°C into 50 mM NaPi, pH 7.4. The CD spectrums were measured on protein samples with concentrations of 15 μM, 10 μM or 1 μM for PSD-95 PDZ1, PSD-95 PDZ1-2 and PSD-95, respectively. Three accumulated scans were acquired for far-UV spectrum at 260-190 nm at 25°C, and 95°C directly followed by a 25°C scan to assess the refolding of the protein, and at 25°C in 6 M urea. Spectra for thermal denaturation were recorded at 260-190 nm from 20-95°C with 5°C intervals. All recorded CD data was obtained in millidegrees and converted to the molar ellipticity constant [θ], deg • cm^2/dmol. The unit was converted based on the mean residual weight, pathlength and protein concentration. The data was analyzed using GraphPad Prism.

Peptide synthesis

Manual peptide synthesis. Unless otherwise stated, amino acids and reagents were purchased from either Iris Biotech or Sigma Aldrich. Peptides were synthesized by SPPS using a 9-fluorenylmethyloxycarbonyl (Fmoc)-strategy at 0.1 mmol scale. Pre-loaded ChemMatrix resins (Sigma Aldrich) were used. Standard coupling reactions were achieved with 1:4:4:8 [resin: N-protected amino acid (AA): 2-(1-benzotriazole-1-yl)-1,1,3,3-tetramethyluronium hexafluorophosphate (HBTU), *N*,*N*-diisopropylethylamine (DIPEA)] or 1:4:4:8 [resin: AA: 1-(bis(dimethylamino)methylene]-1*H*-1,2,3-triazolo(4,5-b)pyridinium 3-oxid hexafluorophosphate (HATU): collidine]. Coupling reactions were agitated at room temperature (RT) and monitored using a Kaiser test kit (Sigma Aldrich). De-protections were carried out with 20% piperidine (2 × 2 min). After coupling or de-protection steps the resin was extensively washed with dimethylformamide (DMF).

Automated peptide synthesis. Automated peptide synthesis using Fmoc-based SPPS was carried out on a Prelude X, induction heating assisted, peptide synthesizer (Gyros Protein Technologies, Tucson, AZ, USA) with 10 mL glass reaction vessel using preloaded Wang-resins (100–200 mesh). Reagents were prepared as solutions in DMF: Fmoc-protected AA (0.2 M), *O*-(1*H*-6-Chlorobenzotriazole-1-yl)-1,1,3,3-tetramethyluronium hexafluorophosphate (HCTU, 0.5 M), and DIPEA (1.0 M). Sequence elongation was achieved using the following protocol: deprotection (2 × 2 min, rt, 300 rpm shaking) and coupling

(2 × 5 min, 75°C, 300 rpm shaking, for Arg and His couplings 2 × 5 min, 50°C, 300 rpm shaking). Amino acids were double coupled using amino acid/HCTU/DIPEA (ratio 1:1.25:2.5) in 5-fold excess over the resin loading to ensure efficient peptide elongation.

TAMRA coupling. N-terminal labelling of peptides with 5-(and-6)-carboxytetramethylrhodamine (TAMRA, Anaspec Inc.) was performed on resin, by coupling TAMRA for 16 h at rt using a mixture in NMP of TAMRA:benzotriazol-1-yloxy)tripyrrolidinophosphonium hexafluorophosphate (PyBOP):DIPEA (1.5:1.5:3) (Witte et al., 2013). To avoid photo bleaching of the fluorophore, the reaction vessel was covered and the coupling finalized with extensive resin washes with DMF and DCM.

Cleavage and purification. Peptides were cleaved from the resin using a mixture of 95:2.5:2.5 (trifluoroacetic acid (TFA), H_2O and triisopropylsilane (TIPS)) for 2 hours at RT. After cleavage the peptides were precipitated in ice-cold diethyl ether. The precipitate was centrifuged 4350 rpm, 10 min, 4°C, washed with cold diethyl ether and the centrifugation step was repeated. The resulting peptide precipitate was dissolved in 50:50:0.1 (MeCN, H_2O, TFA), filtered and lyophilized. All peptides were purified to >95% purity using a preparative RP-HPLC system with a reverse phase C18 column. A linear gradient from 0-40% using a binary buffer system of H_2O, MeCN, TFA (buffer A: 95:5:0.1; buffer B: 5:95:0.1) at 20 mL/min was used. The purity of the collected fractions was measured at 214 nm on RP-UPLC at 0.45 mL/min and the final peptide products were lyophilized. The final products were further verified on LC-MS and the peptides diluted in 62.5 mM Tris-HCl pH 8 in and stored at 20°C.

Fluorescence polarization

The fluorescence polarization (FP) assays were generally performed as previously described (Pedersen et al., 2017). In brief, binding affinities were measured using a Tecan Safire2 Microplate reader (Tecan) in flat bottom black 384-well plates (Corning Life Science) at 25°C. The assays were conducted in 25 mM HEPES, 150 mM NaCl, pH 8, 1 mM TCEP. The TAMRA-labeled probes were measured at excitation/emission at 530/585 nm and the probe concentration was 200 nM in all FP experiments with C-terminal peptide ligands and 10 nM for AVLX-144. Prior to each measurement the instrumental Z-factor was adjusted to maximum fluorescence and the G-factor was calibrated to give an initial millipolarization (mP) at 20 in the probe reference well. For each binding setup, measurements were repeated 3 times. The obtained saturation curve was subtracted from the background and fitted to a one-sided binding model in GraphPad Prism.

Phase transition sedimentation and imaging assay

Proteins were generally prepared as previously described (Zeng et al., 2018a). Proteins were prepared in buffer containing 50 mM Tris, pH 8.2, 100 mM NaCl, 1 mM EDTA, and 2 mM DTT and pre-cleared via high-speed centrifugations. Proteins were then mixed or diluted with buffer to designed combinations and concentrations. For sedimentation assay, typically, the final volume of each reaction is 100 μL. After 10 min equilibrium at room temperature, protein samples were subjected to sedimentation at 16,873 g for 10 min at 25°C on a table-top temperature-controlled micro-centrifuge.

After centrifugation, the supernatant and pellet were immediately separated into two tubes. The pellet fraction was thoroughly re-suspended with the same buffer to the equal volume as supernatant fraction (typically, to 100 μL). Proteins from both fractions were analyzed by SDS-PAGE with Coomassie blue staining. Band intensities were quantified using the ImageJ software. For imaging assay, protein samples were injected into a homemade flow chamber (comprised of a glass slide sandwiched by a coverslip with one layer of double-sided tape as a spacer) for DIC and fluorescent imaging (Nikon Ni-U upright fluorescence microscope) at room temperature. Glasses were washed by Hellmanex II (Hëlma Analytics) and 2 M NaOH sequentially and thoroughly rinsed with MilliQ H2O before chamber making. During imaging, the chamber was sealed by nail polish to reduce solution evaporation. Image fluorescence intensities were analyzed by the ImageJ software.

Isothermal titration calorimetry (ITC) assay

ITC measurements were carried out on a Microcal VP-ITC calorimeter at 25°C. Proteins used for ITC measurements were dissolved in an assay buffer composed of 50 mM Tris, pH 8.2, 100 mM NaCl, 1 mM EDTA, and 2 mM DTT. High concentration of protein was loaded into the syringe and titrated into the cell

containing low concentration of corresponding interactors (concentrations for each reaction were indicated in the figure legends). For each titration point, a 10 μL aliquot of a protein sample in the syringe was injected into the interacting protein in the cell at a time interval of 2 min. Titration data were analyzed using the Origin7.0 software and fitted with the one-site binding model.

QUANTIFICATION AND STATISTICAL ANALYSIS

Data management and statistical analysis were performed using Excel (Microsoft, Redmond, WA) and GraphPad Prism 8 software (GraphPad Software, San Diego, CA).